Downloaded from lithosphere.gsapubs.org on September 21, 2012

Superimposed extension and shortening in the southern Salinas Basin and La Panza Range, California: A guide to Neogene deformation in the Salinian block of the central California Coast Ranges

Joseph P. Colgan[1,*], Darcy K. McPhee[2], Kristin McDougall[3], and Jeremy K. Hourigan[4]
[1]345 MIDDLEFIELD ROAD, MS 973, U.S. GEOLOGICAL SURVEY, MENLO PARK, CALIFORNIA 94025, USA
[2]345 MIDDLEFIELD ROAD, MS 989, U.S. GEOLOGICAL SURVEY, MENLO PARK, CALIFORNIA 94025, USA
[3]2255 NORTH GEMINI DRIVE, U.S. GEOLOGICAL SURVEY, FLAGSTAFF, ARIZONA 86001, USA
[4]EARTH AND MARINE SCIENCES DEPARTMENT, UNIVERSITY OF CALIFORNIA–SANTA CRUZ, SANTA CRUZ, CALIFORNIA 95064, USA

ABSTRACT

We synthesized data from geologic maps, wells, seismic-reflection profiles, potential-field interpretations, and low-temperature thermochronology to refine our understanding of late Cenozoic extension and shortening in the Salinian block of the central California Coast Ranges. Data from the La Panza Range and southern Salinas Basin document early to middle Miocene extension, followed by Pliocene and younger shortening after a period of little deformation in the late Miocene. Extension took place on high-angle normal faults that accommodated ~2% strain at the scale of the ~50-km-wide Salinian block (oriented perpendicular to the San Andreas fault). Shortening was accommodated by new reverse faults, reactivation of older normal faults, and strike-slip faulting that resulted in a map-view change in the width of the Salinian block. The overall magnitude of shortening was ~10% strain, roughly 4–5 times greater than the amount of extension. The timing and magnitude of deformation in our study area are comparable to that documented in other Salinian block basins, and we suggest that the entire block deformed in a similar manner over a similar time span. The timing and relative magnitude of extension and shortening may be understood in the context of central Coast Range tectonic boundary conditions linked to rotation of the western Transverse Ranges at the south end of the Salinian block. Older models for Coast Range shortening based on balanced fault-bend fold-style cross sections are a poor approximation of Salinian block deformation, and may lead to mechanically improbable fault geometries that overestimate the amount of shortening.

LITHOSPHERE; v. 4; no. 5; p. 411–429; GSA Data Repository Item 2012244 | Published online 7 August 2012 doi: 10.1130/L208.1

INTRODUCTION

The central California Coast Ranges (Fig. 1) are dominated by faults of the San Andreas system, which have accommodated over 300 km of right-lateral slip since the early Miocene (e.g., Powell, 1993). The ranges themselves were formed by ongoing crustal shortening in an ~100-km-wide zone stretching from the San Joaquin Valley to the coast across the San Andreas fault. Understanding how this component of deformation evolved through time is a key factor in understanding how transpression and transtension are accommodated within the San Andreas system, while knowledge of local fault geometries is important for understanding natural resources and earthquake hazards within the seismically active central Coast Ranges. Although modern rates of shortening within the Coast Ranges are an order of magnitude less than rates of strike slip (e.g., Argus and Gordon, 2001), damaging earthquakes also occur

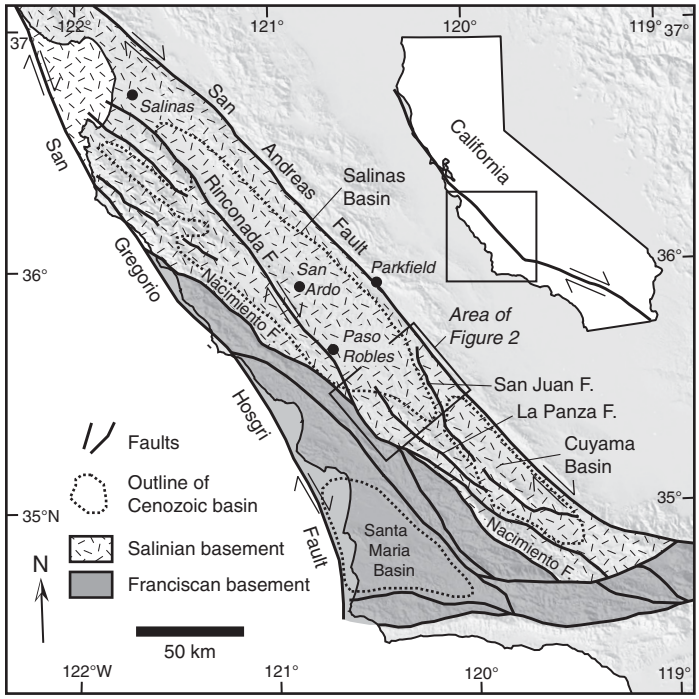

Figure 1. Sketch map of central California coast, showing major faults, extent of Salinian block, major Neogene basins, and location of the study area (derived from Jennings et al., 2010).

*E-mail: jcolgan@usgs.gov.

For permission to copy, contact editing@geosociety.org | © 2012 Geological Society of America

Downloaded from lithosphere.gsapubs.org on September 21, 2012

on thrust or reverse faults, many of which are poorly mapped or even unrecognized (e.g., the Coalinga [M 6.7, 1983] and San Simeon [M 6.5, 2003] earthquakes). Cenozoic Coast Range basins (Fig. 1) also hold important petroleum resources (e.g., San Ardo, Fig. 1), and their stratigraphy and structure are directly related to the way in which deformation is accommodated off the major strike-slip faults in the San Andreas system.

Two distinctly different basement provinces underlie the central Coast Ranges. The Salinian block consists of Cretaceous granitic and metamorphic rocks (and their Cretaceous to Early Tertiary sedimentary cover) that were part of the Mesozoic batholith in southern California prior to northward displacement along the San Andreas fault (e.g., Page et al., 1979; Dickinson, 1983; Jacobson et al., 2011). Southwest of the Nacimiento fault (Fig. 1), the Coast Ranges are underlain by the Franciscan complex and scattered remnants of Jurassic ophiolite. Thick sections of marine sedimentary rocks were deposited in the Salinas, Cuyama, and Santa Maria Basins (Fig. 1) during Miocene transtensional slip on the San Andreas fault (e.g., Graham, 1978), but the magnitude and structural style of extension are poorly known, as is the timing of the transition to more recent crustal shortening.

Neogene deposits throughout the central Coast Ranges were deformed by crustal shortening that mostly took place after 4 Ma, although it may have begun in the late Miocene. Documented shortening perpendicular to the San Andreas fault is roughly 20%–40% strain (e.g., Namson and Davis, 1990; Page et al., 1998), but those areas underlain by Salinian basement (such as the Salinas Basin) appear less deformed than those underlain by Franciscan basement (e.g., Graham, 1987; Titus et al., 2011). Shortening is manifested by folds and thrust faults, but different models exist for the nature of these faults at depth; one set of models emphasizes strike-slip faults that sole into—or are cut by—low-angle detachment faults (e.g., Davis et al., 1988; Namson and Davis, 1988a, 1990), while geophysical data sets point to generally steeply dipping strike-slip faults that cut through the full thickness of the brittle crust and at least locally extend even deeper (e.g., Parsons et al., 2002; Hardebeck, 2010; Shelly, 2010; Fuis et al., 2012). There is also the question of whether extension/shortening in a given area is controlled more by the overall geometry of the Pacific–North American plate margin (e.g., Argus and Gordon, 2001), or by more localized effects of the major strike-slip faults, such as the presence of constraining/releasing bends (e.g., Wakabayashi et al., 2004), or transitions from creeping to locked behavior (e.g., Titus et al., 2011).

The overall goal of this study is to clarify the timing and structural style of Neogene deformation in the Salinian block, which makes up about two thirds of the area of the central Coast Ranges west of the San Andreas fault (Fig. 1). When did the extension begin and end, how much extension took place, and by what structures was it accommodated? Is there a distinct, resolvable transition from extension to shortening, and if so when did this take place? When did most shortening take place, by what structures was it accommodated, and how much overall shortening occurred? To address these questions, we chose to study the central part of the Salinas Basin at the latitude of Paso Robles (Fig. 1). This area offers good exposure of both Mesozoic basement and overlying Cenozoic basin deposits, as well unusually good (for this region) drill-hole and seismic-reflection data from the adjacent basin, much of which has not previously been interpreted in the published literature.

STRATIGRAPHY OF THE SOUTHERN SALINAS BASIN

Salinian basement in the La Panza Range consists of homogeneous granodiorite and quartz monzonite (Ross, 1966). We obtained sensitive high-resolution ion microprobe (SHRIMP) U-Pb dates on zircon from two samples of La Panza granite, one from the SW side of the La Panza fault (sample LP9) and one from the NE side (sample LP3) (Fig. 2). They yielded ages of 79.12 ± 0.46 Ma and 79.36 ± 0.44 Ma, respectively, similar to ages reported by Mattinson and James (1985) from other granites in the southern Salinian block. In the southern La Panza Range, granitic basement is overlain by a S- to SW-dipping sequence of Upper Cretaceous to Paleocene (and possibly early Eocene) sedimentary rocks, predominantly marine turbidites (Vedder and Brown, 1968; Chipping, 1972; Grove, 1993 [Fig. 2]). Vedder and Brown (1968) measured up to 6 km of these strata in the study area, and we initially estimated 4 km based on projected dips from geologic maps. Gravity data indicate a bulk thickness of 1 km at most, however. The reason for this discrepancy is unclear, but because it is peripheral to the focus of this paper, we do not consider it further here.

Granitic basement and older sedimentary rocks are locally overlain by up to 200 m of nonmarine conglomerate and sandstone of the Oligocene (Zemorrian) Simmler Formation (Dibblee, 1973a; Bartow, 1978). It consists predominantly of granitic detritus shed from Cretaceous basement and has been interpreted to record Oligocene slip on normal faults, including an early La Panza fault (Ballance et al., 1983; Ballance, 1984; Yeats et al., 1989). The Simmler Formation and Cretaceous granite are overlain unconformably by marine sandstone and lesser conglomerate of the early Miocene (Saucesian) Vaqueros Formation (Figs. 2 and 3) (Dibblee, 1973a; Bartow, 1974). It is ~50–100 m thick on the NE flank of the La Panza Range (Fig. 2), and thickens in the subsurface from a few meters in the NE part of Figure 2 to over 500 m in the SE. Addicott et al. (1980) interpreted shelfal depths for the Vaqueros Formation in outcrop on the NE flank of the La Panza Range and paleontologic data from the subsurface in our study area to indicate upper bathyal Saucesian depths (150–500 m) that increase to the SW and NW.

The Miocene Monterey and Santa Margarita Formations together form the thickest and most extensive Tertiary sequence in the study area. The Monterey Formation includes siltstone, siliceous shale, diatomite, and chert (Dibblee, 1973a). It ranges from 150 to 500 m thick and generally thickens from SE to NW across the area of Figure 2, ultimately reaching more than 2000 m near the San Ardo oil field, 50 km north of the study area (Fig. 1) (Graham, 1978). In our study area, the Monterey Formation is mostly Relizian and Luisian (17.5–14 Ma) but ranges

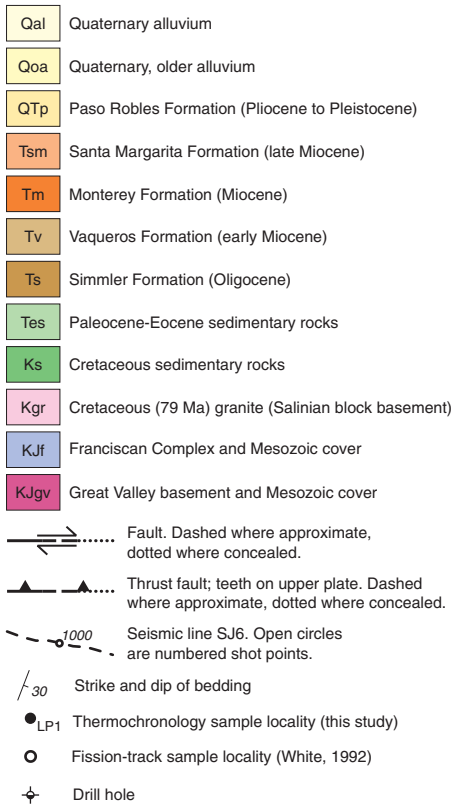

Figure 2 (*continued on following page*).

Downloaded from lithosphere.gsapubs.org on September 21, 2012

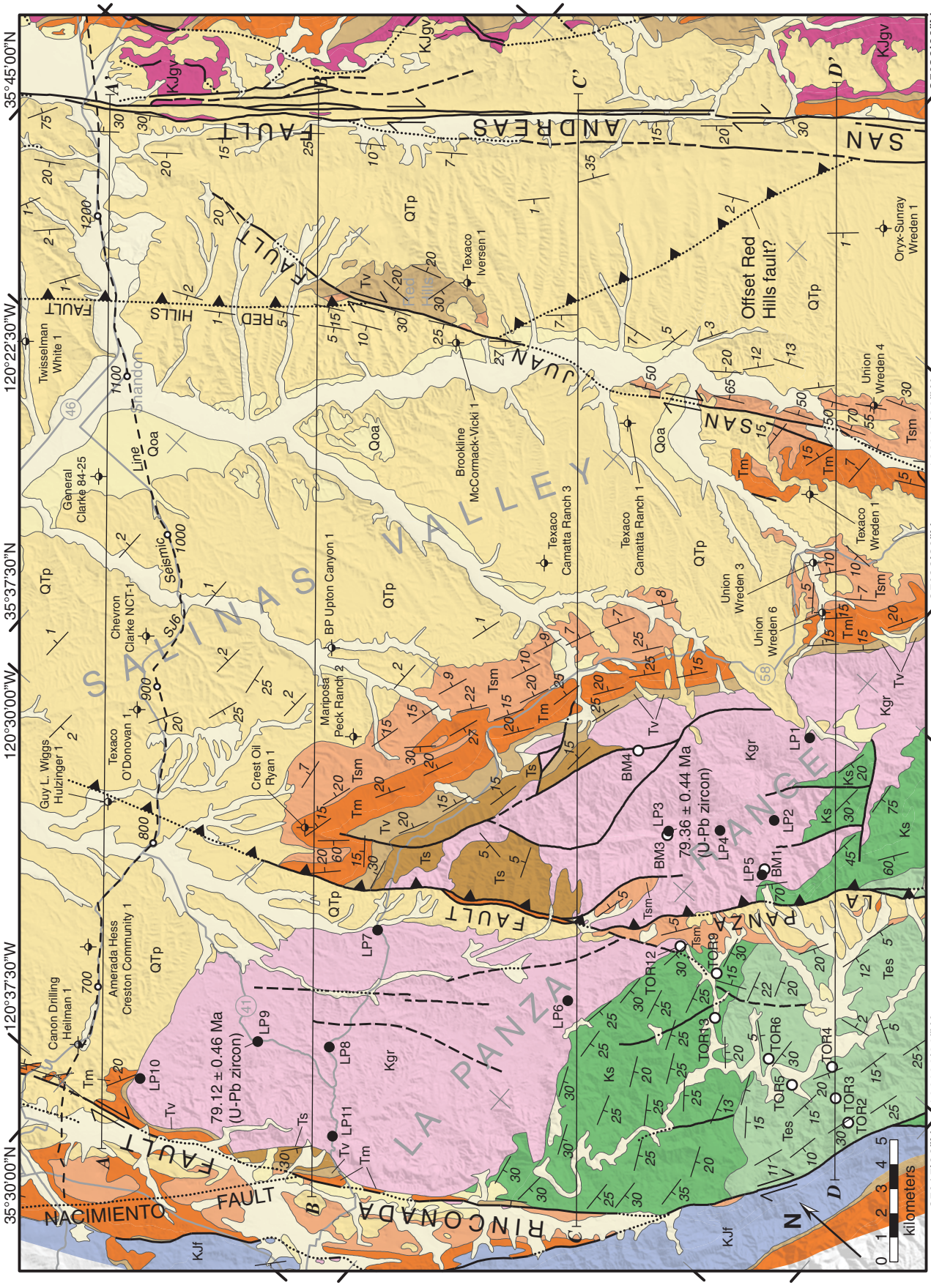

Figure 2 (*continued*). Geologic map of the La Panza Range and southern Salinas Basin, modified from Dibblee (1973b). Tertiary formation names apply only to units between the San Andreas and Rinconada faults; units east of the San Andreas fault are colored the same as their age-equivalents west of the fault but were not deposited in the same basin(s). Age-equivalent Tertiary units west of the Rinconada fault are similarly colored and may or may not share a depositional history with units on the east side of the fault.

Downloaded from lithosphere.gsapubs.org on September 21, 2012

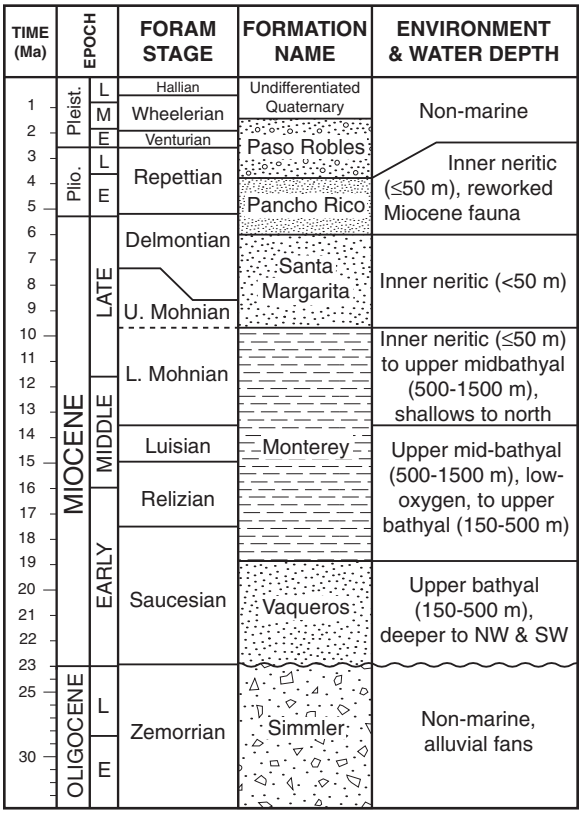

Figure 3. Oligocene and younger stratigraphy of the southern Salinas Basin. Formation names are discussed in text. Age and paleoenvironment assignments are based on re-interpretation of oil company paleontologic data (lists of species from individual samples) from wells in the area of Figure 2 (raw data published by Brabb, 2011). Benthic foraminifer stage and age framework are from McDougall (2007). Complete data sets for individual wells are available in the GSA Data Repository Table DR1[1].

from latest Saucesian to Mohnian (ca. 19–10 Ma). Paleontologic data from outcrops and wells in the study area indicate that the Monterey Formation was deposited at upper bathyal (150–500 m) to upper midbathyal (500–1500 m) depths accompanied by low-oxygen conditions in the Relizian and Luisian (Fig. 3), followed by more variable midbathyal to inner neritic conditions in the Lower Mohnian (Fig. 3). A single occurrence of shelfal (≤150 m) macrofossils at the base of the Monterey Formation was noted by Addicot (1978), but this is unsupported by additional outcrop or subsurface data. Fine-grained siliceous rocks of the Monterey Formation are overlain in the study area by 400–500 m of light-colored, massive- to thick-bedded sandstone assigned to the Santa Margarita Formation by Dibblee (1973a). It is predominantly arkosic, suggesting a source in granitic Salinian basement (Hart, 1976). North of our study area, it is laterally equivalent to the upper part (Hames Member) of the Monterey Formation (Durham, 1974; Graham, 1978), but for convenience, we follow Dibblee (1973a) and show it overlying the Monterey Formation in Figure 2. The Santa Margarita Formation is Upper Mohnian and Delmontian (ca. 13–6 Ma; Fig. 3), and paleontologic data indicate significantly shallower inner neritic (<50 m) conditions (Fig. 3) than for the underlying Monterey Formation.

The Santa Margarita Formation is overlain in the subsurface by 200–500 m of shale, siltstone, and sandstone corresponding to a distinctive low-resistivity interval on electric logs (Fig. 4). We interpret the base of this unit to be the late Miocene (ca. 6 Ma) regional unconformity documented by Barron (1986) at the top of the Monterey Formation (which regionally includes the Santa Margarita Formation). Paleontologic data indicate a shallow-marine environment for this unit (Fig. 3), and the presence of *Elphidiella hannai* and *Elphidium hughesi* demonstrate that it extends into the early Pliocene. Based on lithology and stratigraphic position alone, this unit would most likely correlate with the Pancho Rico Formation, a shallow-marine siltstone that overlies the Santa Margarita Formation over much of the Salinas Basin to the north of our study area (Durham and Addicot, 1965). Although Durham and Addicot (1965) initially assigned an early Pliocene age to the Pancho Rico Formation, it was subsequently revised to be *entirely* late Miocene (Addicot, 1978; Addicot, 1978), which would preclude correlation with the unit in our study area. Either the age reassignment of the Pancho Rico Formation to late Miocene is incorrect, or the top of it is younger in our study area. With this caveat in mind, we use the name "Pancho Rico Formation" for this unit in our study area.

Most of the Salinas Basin in the area of Figure 2 is covered by nonmarine sandstone and conglomerate of the Paso Robles Formation (Fig. 2) (Galehouse, 1967; Dibblee, 1973a). Only an ~100 m section is exposed, but it is very thick in the subsurface near Shandon in the eastern corner of Figure 2—1200 m thick according to Dibblee (1973a), ~730 m according to a recent groundwater study (San Luis Obispo County Water Resources Division of Public Works, 2005), and ~1000 m thick according to this study (Fig. 4). Different interpretations probably arise from difficulty in picking the gradational basal contact in well logs; we place it at the top of the low-resistivity interval correlated with the Pancho Rico Formation (Fig. 4). Galehouse (1967) argued for a middle to late Pliocene Paso Robles Formation based on the early Pliocene age of the underlying Pancho Rico Formation, while Dibblee (1973a) contended that it was mostly Pleistocene because it locally overlies early Pliocene rocks on an angular unconformity. A more recent study of the Paso Robles Formation based on extensive well data also found the basal contact to be an angular unconformity developed locally on the Pancho Rico Formation (San Luis Obispo County Water Resources Division of Public Works, 2005). Here, we assume the Paso Robles Formation to be late Pliocene and Pleistocene (Fig. 3). Galehouse (1967) noted that the Paso Robles Formation contains abundant porcelainite pebbles reworked from the Monterey Formation, with the remainder of clasts sourced from granitic basement and undifferentiated Cretaceous and Tertiary sandstones.

STRUCTURE OF THE LA PANZA RANGE AND SOUTHERN SALINAS BASIN

Subsurface basin geometry and major structures in the study area can be documented using data from geologic maps, wells, seismic profiles, and potential-field interpretation. Drill-hole data are publicly available from the State of California Division of Oil, Gas, and Geothermal Resources (DOGGR), and Brabb (2011) published paleontologic data (lists of species with age calls) from select wells. Seismic-reflection line SJ-6 (Fig. 2) was collected and processed by Western

[1]GSA Data Repository Item 2012244, description of foraminifers in selected wells from the southern Salinas basin, compiled from notes on electric logs with updated taxonomy and age interpretations, is available at www.geosociety.org/pubs/ft2012.htm, or on request from editing@geosociety.org, Documents Secretary, GSA, P.O. Box 9140, Boulder, CO 80301-9140, USA.

Downloaded from lithosphere.gsapubs.org on September 21, 2012

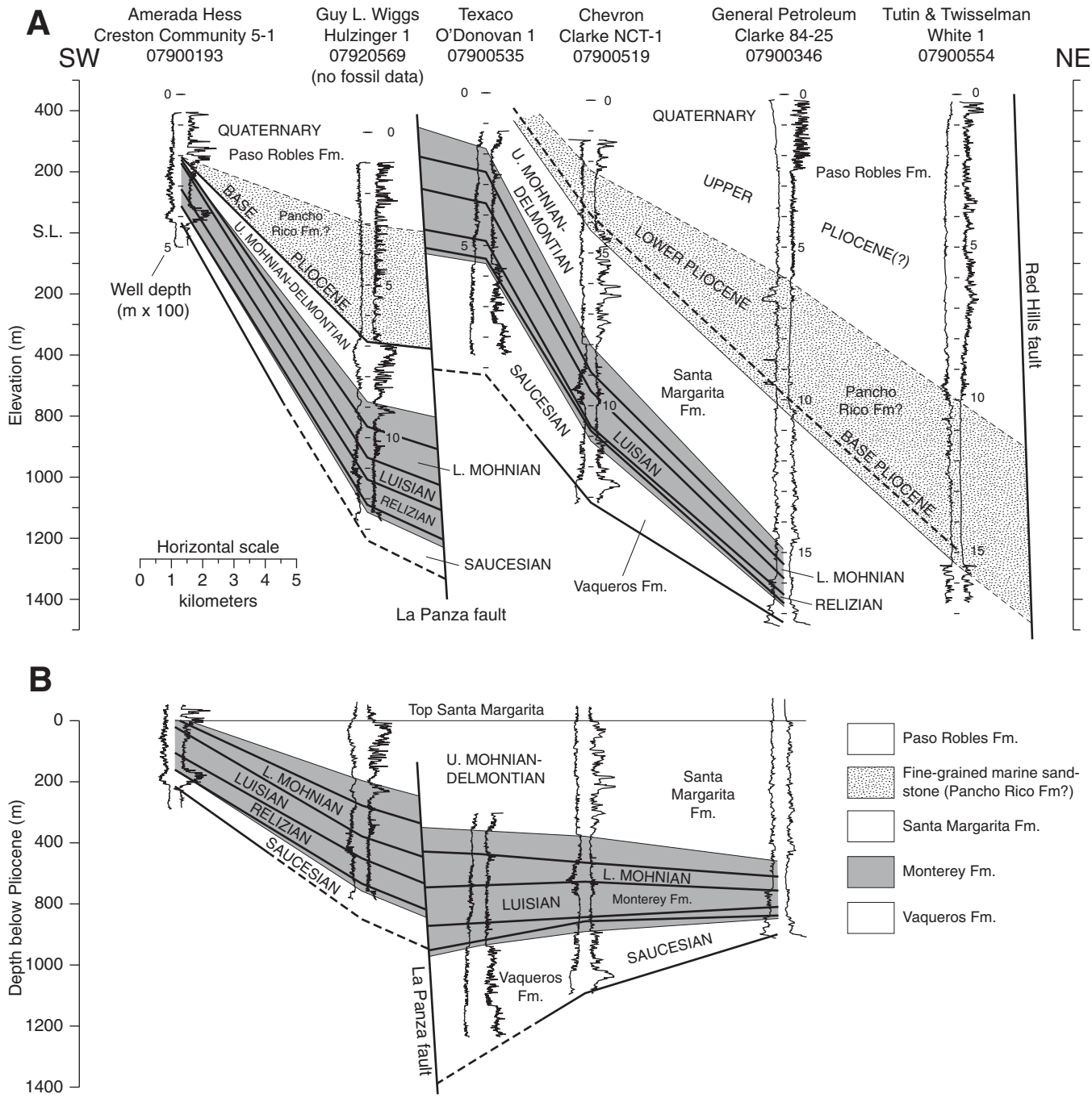

Figure 4. (A) SW-NE stratigraphic section across the southern Salinas Basin, approximately coincident with cross section A-A′ and seismic-reflection line SJ6 (Fig. 2). Note that "La Panza fault" is actually multiple faults in a zone ~2 km wide. (B) Same section flattened on top of Santa Margarita Formation, showing increase in thickness of lower part of section across La Panza fault. Spontaneous potential (left curve)/resistivity (right curve) logs are from unpublished records held by the California Division of Oil, Gas, and Geothermal Resources. American Petroleum Institute (API) numbers are given beneath well names. Benthic foraminifer stages are as shown in Figure 3.

Geophysical Company in 1981, and the U.S. Geological Survey acquired the rights in 1983. Trehu and Wheeler (1987a, 1987b) published an interpretation of deep crustal structure based on a version of this record reprocessed to 12 s, but the shallow subsurface record across the Salinas Basin has not been interpreted in the published literature. In this study, a Mylar printout of the original migrated 6 s record was interpreted visually, with approximate depth to reflectors calculated from RMS (root mean square) velocities specified on the printed record.

Gravity stations are unevenly distributed throughout the region, with an average spacing of 1 station per 1.6 km^2 (Fig. 5). Stations were compiled from various sources including McPhee et al. (2011), Burch et al. (1971), Campion et al. (1983), and the former Defense

Downloaded from lithosphere.gsapubs.org on September 21, 2012

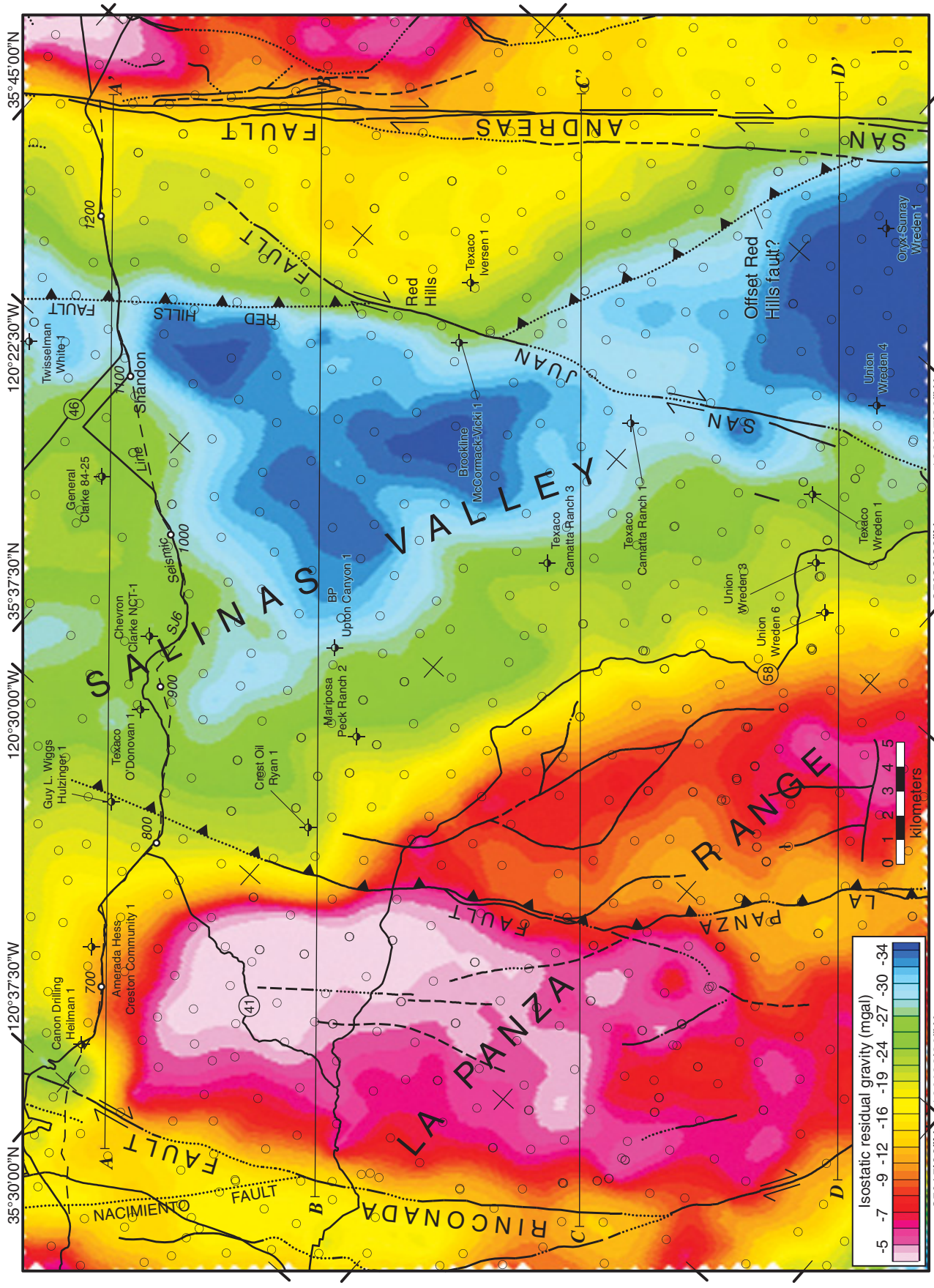

Figure 5. Isostatic residual gravity map of the La Panza Range and southern Salinas Valley. Geologic and cultural features are same as Figure 2. Black open circles are gravity stations. Data sources are listed in text.

Downloaded from lithosphere.gsapubs.org on September 21, 2012

Mapping Agency. Observed gravity values were referenced to the International Gravity Standardization Net 1971 gravity datum (Morelli, 1974). Details of gravity data processing can be found in McPhee et al. (2011). Average densities used here for gravity modeling are: 2300 kg/m^3 for Oligocene and younger sedimentary basin fill, 2560 kg/m^3 for Cretaceous to Paleocene sedimentary rocks, and 2670 kg/m^3 for Mesozoic basement (Fig. 6). These values are based on density measurements of relevant units throughout the California Coast Ranges (V.E. Langenheim, 2011, personal commun.) and published velocity and density logs from the Neogene sedimentary basins (Brocher, 2005).

San Andreas, Rinconada, and Nacimiento Faults

The Salinian block at the latitude of the study area is bounded on the northeast by the San Andreas fault (Figs. 1 and 2). Earthquakes and deep seismic tremors collocated with the surface trace of the San Andreas fault in the area of Figure 2 demonstrate that it cuts the crust vertically to a depth of ~25 km—essentially to the Moho (e.g., Thurber et al., 2006; Shelly, 2010). This strand of the San Andreas fault has an estimated 300–320 km of right-lateral offset since the beginning of the Miocene, which would restore the study area to southern California at the end of the Oligocene (e.g., Graham, 1989; Powell, 1993). The San Andreas fault is currently slipping ~20–30 mm/yr in the area of Figure 2 (Toké et al., 2011). Because it is such a large (600-km-long), rapidly moving structure that vertically cuts the entire thickness of the crust, we judge that the San Andreas fault is not—and has not been—cut and displaced by gently dipping thrust or detachment faults (e.g., Namson and Davis, 1988a, 1988b, 1990).

The Salinian block is bounded on the southwest by the Nacimiento fault (Figs. 1 and 2), which separates it from Franciscan basement (e.g., Page, 1970). There is controversy over the timing (Cretaceous vs. Tertiary, or both) and nature of slip (thrust vs. strike slip) on the Nacimiento fault, but it is clearly pre-Miocene (Dickinson, 1983; Vedder et al., 1991; Ducea et al., 2009; Jacobson et al., 2011). In the area of Figure 2, the Nacimiento fault is offset or reactivated by the right-lateral Rinconada fault (Dibblee, 1976; Page et al., 1979), which now forms the principal boundary between Salinian and Franciscan basement in our study area. Estimates of post-Oligocene right-lateral slip on the Rinconada fault range from 60 km (Dibblee, 1976) to ~45 km (Graham, 1978; Grove, 1993). There is evidence for Quaternary slip, but no Holocene offset has been documented (Rosenberg and Clark, 2009). Hardebeck (2012) interpreted earthquakes in the Paso Robles area to reflect right-lateral strike slip on a steeply SW-dipping Rinconada fault, while recent modeling (V.E. Langenheim, 2011, personal comm.) found that a steeply (~78°) NE-dipping Rinconada fault was required to model the aeromagnetic anomaly over the fault. In either case the Rinconada fault is steeply-dipping in the upper crust.

San Juan and Red Hills Faults

Dibblee (1976) mapped the San Juan fault (Fig. 2) as a steeply dipping right-lateral strike-slip fault subparallel to the San Andreas fault. Where it bounds the southwest side of the Red Hills (Fig. 2), this fault is the same as Ross' (1966) "Red Hills fault." Subsequent workers have used both names; we use the name "San Juan fault" to refer to the high-angle strike-slip fault southwest of the San Andreas fault in the area of Figure 2. The San Juan fault likely intersects the San Andreas at the eastern end of section A-A′, but this intersection has not actually been mapped (Dibblee, 1976). Bartow (1974) estimated 13–15 km of post-Oligocene right-lateral offset on the San Juan fault, and Dibblee (1976) suggested 13 km of right-lateral offset since the early Pliocene.

We propose that the name "Red Hills fault" be reserved for a NE-dipping, SW-vergent thrust fault ~8 km southwest of the San Andreas fault (Figs. 2 and 6). This fault is only apparent in seismic and gravity data and to our knowledge has not been documented in the published literature. Figure 7 shows a seismic-reflection image of the Red Hills fault, which is clearly visible as a moderately dipping thrust fault that has uplifted Oligocene rocks exposed in the Red Hills and in the "Iversen 1" drill hole (Figs. 2 and 6). A drill hole 1 km SW of the Red Hills fault (Twisselman "White" 1; Figs. 2 and 4) encountered the top of the Santa Margarita Formation at ~1550 m. Based on electric logs (Fig. 4) and interval velocities specified for that portion of the seismic record, we assign this contact to a prominent reflector at ~1.1 s or roughly 1500 m (Fig. 7). Tracing this reflector to its intersection with the fault plane yields a fault dip of ~37°, and repeating this exercise for the inferred base of the Paso Robles Formation yields a fault dip of ~30°. The best-fit model of the gravity data over the Red Hills fault yielded a 31° dip for the fault. The closest drill hole to the Red Hills fault that hit basement in its footwall ("Clarke" 84–25; Fig. 2) encountered ~690 m of Miocene and Oligocene strata; if we assume a similar thickness beneath the Pliocene in "White 1," we get a depth to basement of 2240 m. Gravity modeling (Fig. 6A) indicates a comparable depth to basement of ~2400 m in the footwall of the Red Hills fault, and ~800 m in the hanging wall, which gives ~2800 m of NW-SE shortening (assuming a 35° dip) on the Red Hills fault on section A-A′ (Fig. 6A).

Along C-C′ and D-D′ (Fig. 6), there is no significant gravity gradient across the San Juan fault, consistent with very limited vertical basement offset. The prominent basement gravity high in the hanging wall of the Red Hills fault strikes south to intersect the map trace of the San Juan fault at the north end of the Red Hills (Fig. 5). Along B-B′, the gravity gradient across this intersection is much too steep to model with a 30°–35° dipping thrust (Fig. 6B). A vertical fault is required, with a modeled ~2 km of up-to-the-NW basement offset (Fig. 6B). Given the lack of vertical basement offset on the San Juan fault elsewhere, we surmise that the Red Hills fault displaced basement up to the NW prior to being cut obliquely by the vertical San Juan fault. A younger San Juan fault is consistent with mapped deformation in the Paso Robles Formation, which is tilted 20°–30° at the surface near the San Juan fault, but which is undeformed over the surface trace of the Red Hills fault (Fig. 2). If the displaced southern segment of the Red Hills fault follows the edge of the basement gravity high between the San Andreas and San Juan faults (Fig. 5), it would be offset ~5–10 km along the San Juan fault (Fig. 2).

La Panza Fault

The La Panza fault is a NE-dipping, NW-striking thrust fault that divides the La Panza Range into eastern and western halves (Fig. 2) (Dibblee, 1976), which we refer to as the "eastern" and "western" La Panza Range in this paper. The La Panza fault cuts the Paso Robles Formation and was interpreted by Dibblee (1976) to have Pleistocene slip. Ballance (1984) and Yeats et al. (1989) argued for Oligocene normal slip on the La Panza fault during deposition of the Simmler Formation. There are no published estimates of the amount of dip-slip offset on the La Panza fault. Durham (1974) argued for 7–8 km of right-lateral slip, and Balance et al. (1983) proposed up to 50 km of right-lateral slip based on apparent offset of the Simmler Formation. Continuity of the E-trending Cretaceous unconformity across the La Panza fault (Fig. 2) rules out more than ~1 km of right-lateral slip, however (Dibblee, 1976).

The La Panza fault is a blind thrust in the subsurface along A-A′ (Fig. 6A). The fault itself is not visible in seismic data, but an overlying SW-vergent fold involving Pliocene and Pleistocene rocks is clearly evident (Fig. 8). About 2 km to the NE, another unnamed

Downloaded from lithosphere.gsapubs.org on September 21, 2012

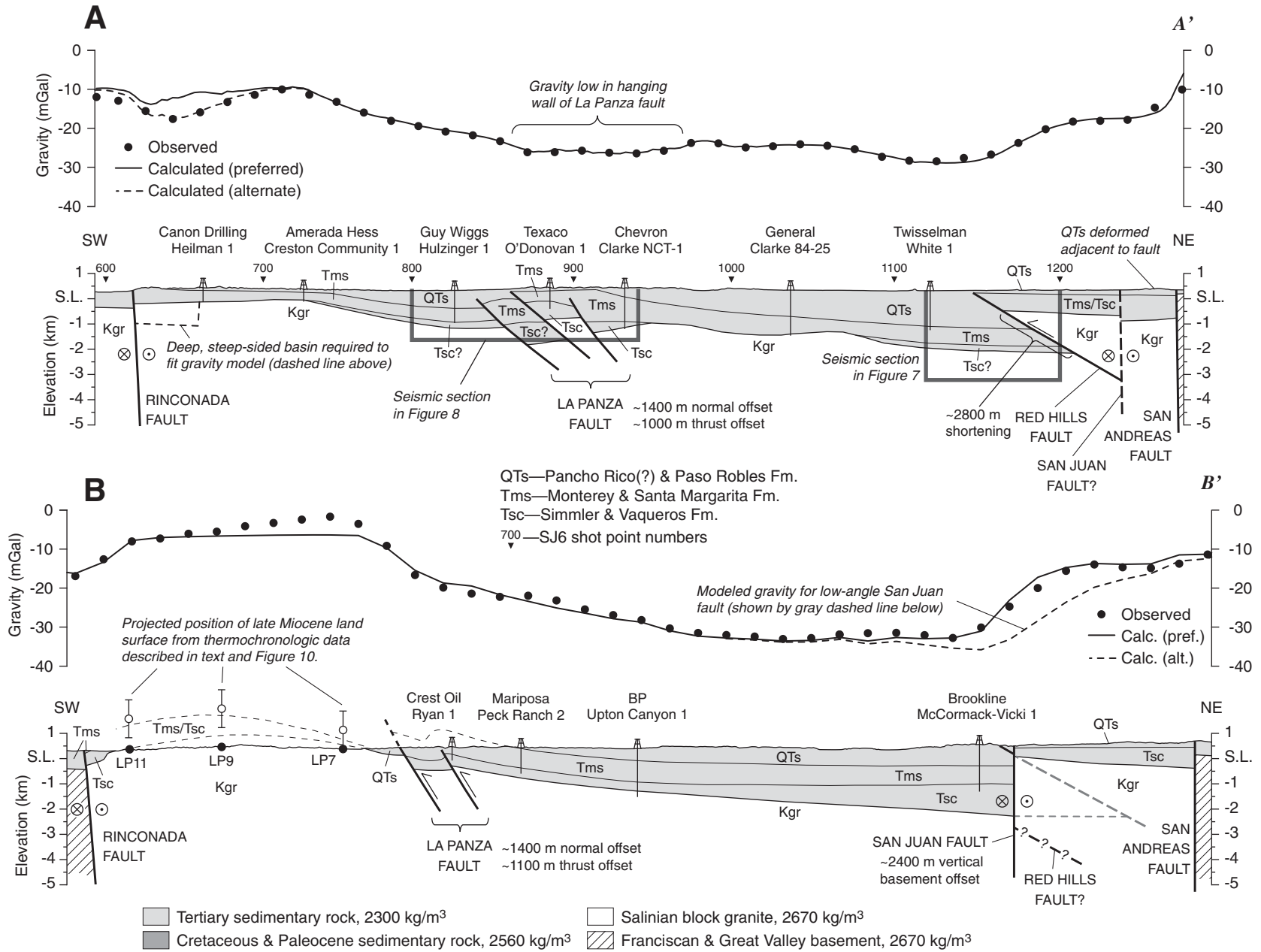

Figure 6. Geologic cross sections and modeled gravity profiles. Locations of sections are in Figures 2 and 5. S.L.—sea level. (*Continued on following page.*)

Downloaded from lithosphere.gsapubs.org on September 21, 2012

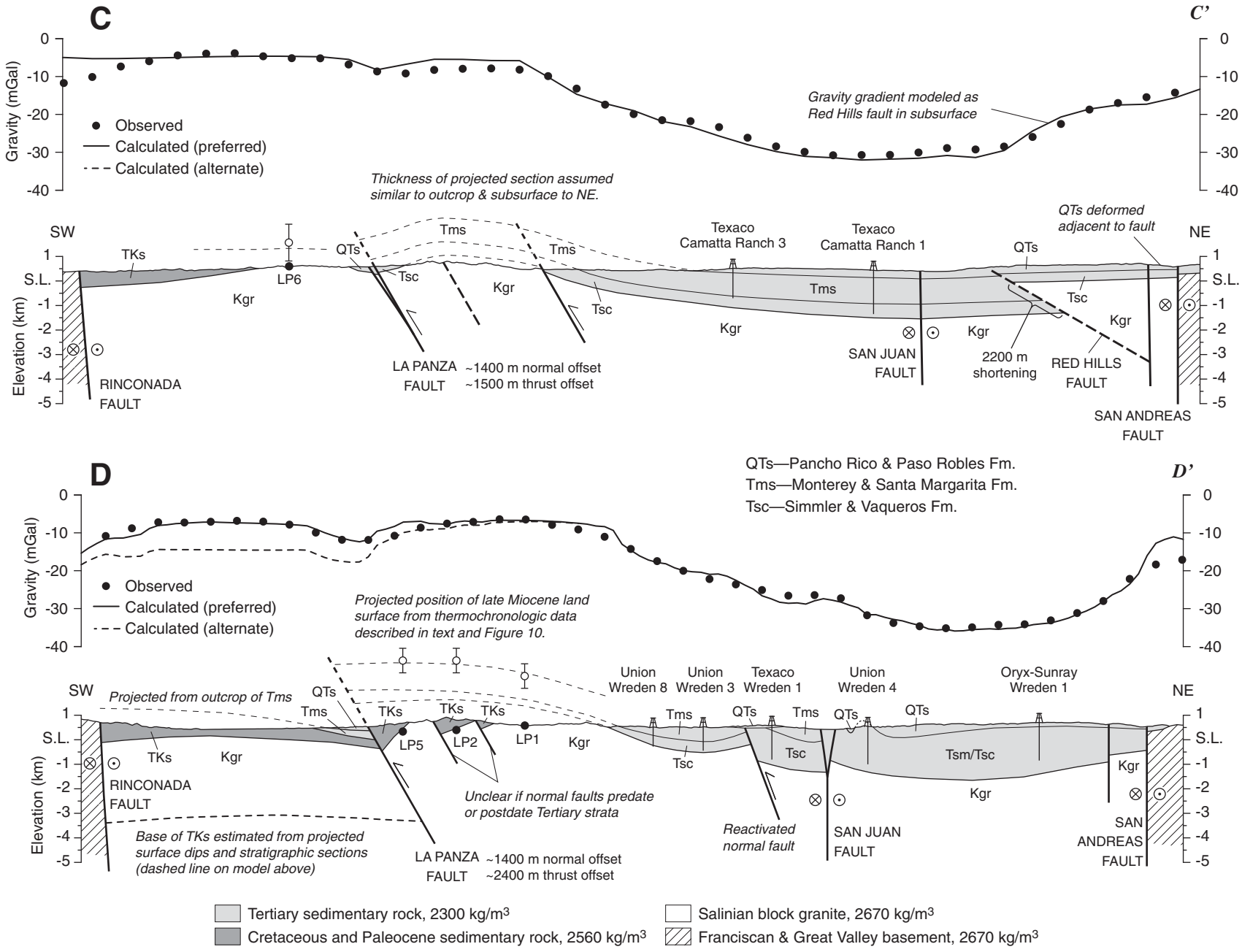

Figure 6 (*continued*).

Downloaded from lithosphere.gsapubs.org on September 21, 2012

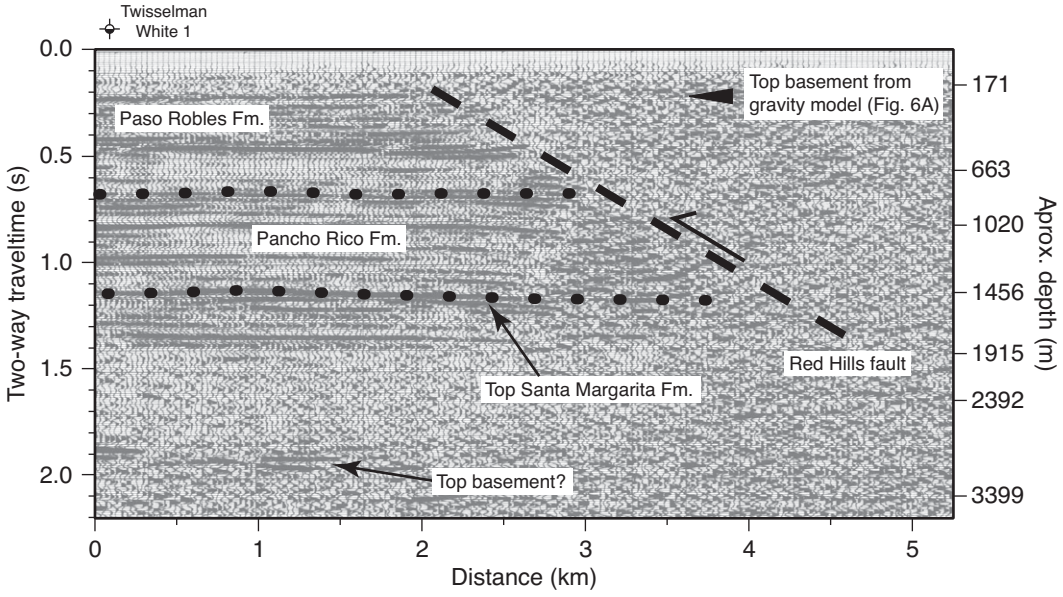

Figure 7. Seismic-reflection line SJ6 across the Red Hills fault (shot point 1120-1200). Heavy dotted lines are stratigraphic contacts; heavy black dashed line is Red Hills fault. Depths are calculated from root mean square (RMS) velocities west of the Red Hills fault.

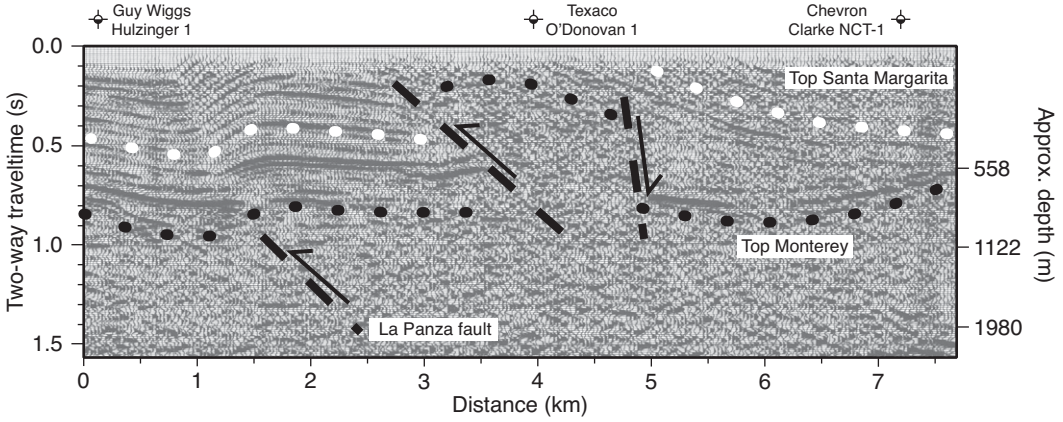

Figure 8. Seismic-reflection line SJ6 across the La Panza fault (shot point 820-940). Heavy black dotted line is top of Monterey shale; heavy white dotted line is top of Santa Margarita Formation; heavy black dashed lines are faults. Depths are calculated from root mean square (RMS) velocities east of the La Panza fault.

thrust fault is clearly visible in the seismic data (Fig. 8), over which the Paso Robles Formation is folded at the surface (Fig. 2). Together, this fault and the La Panza fault—which we consider part of the same fault system—offset the top of the Monterey Formation ~700 m (up to the NE) between the "Hulzinger 1" and "O'Donovan 1" drill holes (Figs. 2, 4, and 8), with the majority of offset on the unnamed NE fault. Despite a clear up-to-the-NE sense of slip on the La Panza fault, the gravity gradient across the fault clearly indicates basement offset *down* to the NE (Figs. 5 and 6), consistent with a thicker Miocene section in its hanging wall deposited during earlier, down-to-the-NE normal slip. A normal-sense growth fault within the lower part of the Santa Margarita Formation is clearly visible in seismic data in Figure 8, ~3 km NE of the La Panza fault.

Along and near B-B′ (Fig. 2), the La Panza fault places Oligocene and Miocene sedimentary rocks over Pliocene to Pleistocene Paso Robles Formation. As along A-A′, the strong gravity gradient over the fault (Fig. 6B) indicates down-to-the-NE basement offset. This is supported by field relationships mapped by Dibblee (2004) in the Wilson Corner 7.5′ quadrangle where section B-B′ crosses the La Panza fault (Figs. 2 and 6). Here, folded Oligocene to Miocene strata are ~1200 m thick in the hanging wall of the La Panza fault but absent in its footwall, where a thin (~100 m) layer of Paso Robles Formation is deposited directly on granitic basement. A second thrust fault ~2 km NE of the La Panza fault dies out up section into the core of a W-vergent fold (Figs. 2 and 6). The Vaqueros Formation and lower part of the Monterey Formation (Saucesian to Relizian) are ~280 m thick in footwall of this fault and ~530 m in the hanging wall, consistent with early to middle Miocene normal slip prior to reactivation as a blind thrust fault.

FISSION-TRACK AND U-Th/He THERMOCHRONOLOGY

Overview and Previous Work

We obtained apatite fission-track and (U-Th)/He data from granitic basement in the La Panza Range in order to investigate differential Miocene burial and exhumation on both sides of the La Panza fault. Fission-track dating is based on the spontaneous fission-decay of ^{238}U, which forms linear damage trails in the host crystal that are progressively erased (annealed) at elevated temperatures (e.g., Tagami and

Downloaded from lithosphere.gsapubs.org on September 21, 2012

O'Sullivan, 2005). In apatite, fission tracks are annealed instantaneously (at geologic time scales) above 110–135 °C, partially annealed between ~120 °C and 60 °C (the "partial annealing zone" or PAZ), and retained over geological time scales below ~60 °C (e.g., Gleadow et al., 1986; Green et al., 1989). Apatite fission-track ages do not correspond to unique time-temperature (*t-T*) paths, but the distribution of confined track lengths within the sample can be inverse-modeled to derive the *t-T* path associated with the measured age (e.g., Green et al., 1989; Ketcham, 2005).

The (U-Th)/He system is based on the α-decay of U and Th, which produces ^{4}He that is lost by thermal diffusion at elevated temperatures (Zeitler et al., 1987; Farley, 2002). In apatite, ^{4}He is completely lost above ~80 °C, partly retained over geologic time scales between 80 and 40 °C (the "partial retention zone" or PRZ), and effectively completely retained below ~40 °C (e.g., Wolf et al., 1996, 1998; Farley, 2000). Time-temperature paths cannot be recovered from individual apatite (U-Th)/He ages, but they provide a very useful constraint on the lower-temperature (<60 °C) part of the *t-T* path when combined with apatite fission-track data from the same sample (e.g., Ketcham, 2005).

White (1992) obtained apatite fission-track ages from 11 samples in the southern La Panza Range (Fig. 2; Table 1). Most were from detrital apatite from the Cretaceous and Lower Tertiary sedimentary rocks, but several were from Cretaceous granite in the southeastern La Panza Range (Fig. 2). Most ages are 50–60 Ma (Table 1), i.e., close to the interpreted depositional age of the Cretaceous to Paleocene sedimentary rocks. White (1992) reported no age trends in these data, either E-W across the La Panza fault or vertically through the Cretaceous–Paleocene section. She interpreted track-length data from her samples to record reheating to 50–80 °C between 42 and 3 Ma (White, 1992). Spotila et al. (2007) reported three apatite (U-Th)/He ages from Cretaceous granite northeast of the La Panza fault that range from 8 to 12 Ma (in the vicinity of our samples LP1 and LP2, Fig. 2), consistent with late Miocene temperatures >60 °C. No (U-Th)/He ages have been reported from the study area between the La Panza and Rinconada faults.

Apatite Fission-Track and (U-Th)/He Data

We collected 11 samples of granite from the La Panza Range for apatite fission-track and (U-Th)/He analysis, six from the west side of the La Panza fault and five from the east side (Fig. 2; Table 1). We sampled the granite because it yields higher-quality apatite than the Cretaceous strata and was buried more deeply than the overlying sedimentary rocks and thus was more likely to preserve a young cooling signal. The goals of this analysis were to refine estimates of Tertiary burial depth of granitic basement and the timing and magnitude of subsequent exhumation, with emphasis on unroofing due to slip on the La Panza fault.

Nine of the 11 La Panza granite samples yielded abundant, high-quality apatite suitable for analysis—euhedral, clear, intact grains largely free of obvious inclusions or other defects (LP8 and LP10 did not). From these samples, we obtained fission-track age and confined track-length data, together with multiple single-grain (U-Th)/He ages (Table 1; Appendixes B and C). Fission-track ages are noticeably older on the west side of the La Panza fault, ranging from 66 to 74 Ma as opposed to 41–68 Ma (mostly around 55 Ma) on the east side (Table 1). The disparity in (U-Th)/He ages is even more pronounced, with ca. 10 Ma ages from east of the La Panza fault versus 35–55 Ma ages from the west side of it (Table 1).

To understand this differential resetting of (U-Th)/He ages, we used the HeFTy algorithm of Ketcham (2005) to model the peak temperature of each sample at the time it was most deeply buried by Miocene sedimentary rocks. All samples were modeled using the same

TABLE 1. LA PANZA RANGE THERMOCHRONOLOGY, SAMPLE LOCALITY, AND AGE DATA

Sample number	Unit (Fig. 2)	Latitude* (°N)	Longitude* (°W)	Apatite FT age† (Ma, ±1σ)	Mean track length (μm, ±1σ) (no. of tracks)	Apatite (U-Th)/He§ age (Ma, ±1σ)	Data source
Samples southwest of La Panza fault							
JC10-LP11	Kgr	35.4122	120.5619	73.6 ± 3.7	13.03 ± 0.10 (*n* = 60)	34.5 ± 1.5	This study
JC10-LP9	Kgr	35.4560	120.5524	70.1 ± 3.6	12.71 ± 0.16 (*n* = 85)	55.3 ± 1.9	This study
JC10-LP6	Kgr	35.3804	120.4459	65.7 ± 3.3	12.96 ± 0.19 (*n* = 63)	37.8 ± 1.3	This study
JC10-LP7	Kgr	35.4502	120.4789	74.3 ± 4.8	13.01 ± 0.12 (*n* = 92)	37.5 ± 1.3	This study
TOR2-87	Tes	35.2737	120.4038	63.0 ± 8.2	12.41 ± 0.44 (*n* = 48)	–	White (1992)
TOR3-87	Tes	35.2828	120.3994	62.6 ± 14.2	13.09 ± 0.29 (*n* = 89)	–	White (1992)
TOR4-87	Tes	35.2914	120.3902	48.7 ± 6.9	13.10 ± 0.29 (*n* = 82)	–	White (1992)
TOR5-87	Tes	35.2984	120.4089	71.0 ± 7.2	13.05 ± 0.21 (*n* = 148)	–	White (1992)
TOR6-87	Tes	35.3111	120.4061	52.7 ± 5.5	13.30 ± 0.29 (*n* = 98)	–	White (1992)
TOR13-87	Ks	35.3361	120.4082	49.9 ± 6.5	13.44 ± 0.37 (*n* = 60)	–	White (1992)
TOR9-87	Ks	35.3463	120.3929	53.4 ± 8.5	13.51 ± 0.99 (*n* = 5)	–	White (1992)
TOR12-87	Kgr	35.3633	120.3944	62.2 ± 7.7	13.59 ± 0.29 (*n* = 90)	–	White (1992)
Samples northeast of La Panza fault							
JC10-LP5	Kgr	35.3574	120.3455	54.3 ± 3.1	9.94 ± 0.21 (*n* = 62)	9.4 ± 0.4	This study
BM1-90	Kgr	35.3587	120.3435	46.0 ± 4.8	12.23 ± 0.46 (*n* = 100)	–	White (1992)
JC10-LP4	Kgr	35.3799	120.3430	52.2 ± 3.2	10.27 ± 0.18 (*n* = 76)	10.4 ± 0.4	This study
JC10-LP2	Kgr	35.3674	120.3234	41.0 ± 2.5	9.21 ± 0.42 (*n* = 48)	11.2 ± 0.4	This study
JC10-LP3	Kgr	35.3940	120.3585	58.3 ± 2.9	11.58 ± 0.11 (*n* = 76)	12.7 ± 0.3	This study
BM3-90	Kgr	35.3944	120.3587	58.2 ± 6.0	13.11 ± 0.46 (*n* = 100)	–	White (1992)
JC10-LP1	Kgr	35.3777	120.2850	67.4 ± 3.1	11.94 ± 0.19 (*n* = 47)	9.6 ± 0.4	This study
BM4-90	Kgr	35.4226	120.3412	53.1 ± 10.0	12.45 ± 1.00 (*n* = 14)	–	White (1992)

Note: FT—fission-track.
*North American Datum of 1927.
†Data from this study are given in Table B1.
§Mean of multiple single-grain analyses; data are given in Table C1.

Downloaded from lithosphere.gsapubs.org on September 21, 2012

geologic constraints (black boxes in Fig. 9) based on stratigraphic relationships described in the text. For example, the presence of Oligocene strata resting unconformably on granitic basement means that basement was close to the surface at that time (box 4, Fig. 9). The one "open" constraint was the magnitude of middle to late Miocene reheating (box 5, Fig. 9), which was allowed to vary over more than the full sensitivity range of the combined fission-track and (U-Th)/He systems in apatite (Fig. 9).

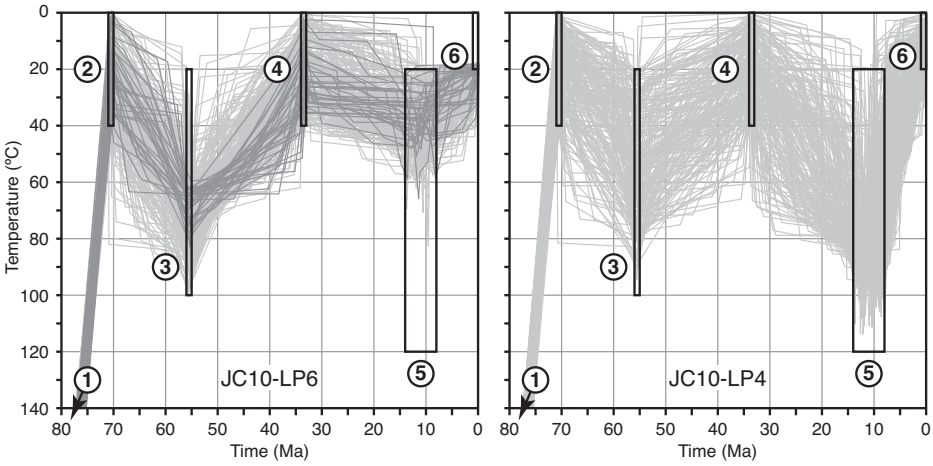

Figure 9. Modeled time-temperature paths for La Panza Range samples JC10-LP6 and JC10-LP4. Model constraints (black boxes) based on geologic data discussed in text are the same for all other samples: (1) crystallization of pluton at 79 Ma; (2) near surface in Late Cretaceous (70 Ma); (3) burial beneath Cretaceous–Early Tertiary sedimentary rocks; (4) near surface in Oligocene (unconformity at base of Simmler Formation); (5) burial beneath variable thickness of Miocene sedimentary rocks ca. 14–8 Ma; and (6) at surface today. Light-gray paths fit model at 95% confidence; dark-gray paths fit at 50% confidence.

Thermal Model Results and Interpretation

Modeled *t-T* paths for samples LP6 and LP4 (west and east of the La Panza fault, respectively) are shown in Figure 9 as representative model results. For both samples, rapid cooling and exhumation of ca. 79 Ma granitic basement prior to deposition of Late Cretaceous strata (boxes 1–2, Fig. 9) would result in initial fission-track and (U-Th)/He ages older than 70 Ma. For sample LP6, the ca. 65 Ma fission-track age still records this initial cooling, although the model prefers to modify it slightly during burial beneath the Late Cretaceous strata. The 38 Ma (U-Th)/He age is partially reset but precludes reheating to >60 °C during the Miocene. In contrast, the 9 Ma (U-Th)/He age from sample LP4 requires that it be reheated to >80 °C in the Miocene (which also partially resets the fission-track age to ca. 54 Ma) prior to rapid cooling around 9–10 Ma. Although plots like Figure 9 make it easy to see the full *t-T* path of a sample, the path density obscures the specific points at which each path passes through the constraint boxes. Figure 10 shows only the "nodes" through which the model requires the *t-T* path to pass during Miocene reheating. From these nodes, we calculated the mean peak Miocene temperature for each sample (Fig. 10), which clearly shows that basement east of the La Panza fault was ~50 °C hotter than it was west of the fault by ca. 10 Ma.

Converting estimated temperatures in Figure 10 to estimated depths in the Miocene crust requires knowledge of the geothermal gradient. Midbathyal to shelfal middle to late Miocene water depths over what would become the La Panza Range correspond to a "surface" temperature of ~5–10 °C. Sample LP1 is the closest to the base of the Miocene section (Fig. 2); assuming it was buried to ~2 km depth (Fig. 6), the modeled reheating temperature of 68 °C ± 8 °C (Fig. 10) indicates a geothermal gradient on the order of 30 ± 5 °C/km. This is comparable to the modern geothermal gradient of 35 °C/km measured in the San Andreas

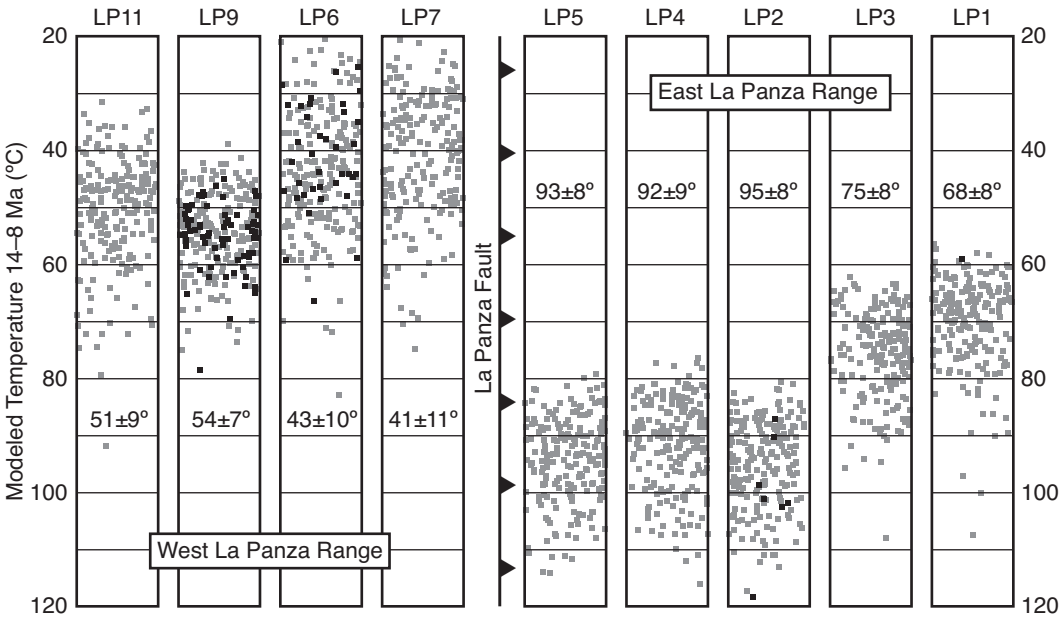

Figure 10. Modeled late Miocene reheating temperatures for La Panza Range thermochronology samples (constraint box 5 from Fig. 9). Black dots are 50% confidence; gray dots are 95% confidence. Average temperature for each sample ±1σ.

Downloaded from lithosphere.gsapubs.org on September 21, 2012

Fault Observatory at Depth (SAFOD) borehole near Parkfield (Fig. 1) (Williams et al., 2005). An elevated middle-late Miocene geothermal gradient is consistent with passage of the Mendocino triple junction slab window beneath the central Salinian block sometime in the early Miocene (e.g., Dickinson, 1997).

Assuming a surface temperature of ~5–10 °C, and geothermal gradient on the order of 30 °C/km, we estimated the position of the late Miocene land surface over each sample (open symbols with error bars in Fig. 6). Higher temperatures equate to slightly deeper burial depths for the part of the eastern La Panza Range closest to the La Panza fault (>90 °C vs. ~70 °C; Fig. 10). This may be due either to exhumation from greater depth in the Mesozoic basement, or to the Tertiary section being thicker there, owing to the presence of growth strata deposited during early normal slip as observed in subsurface data to the north (Fig. 4). The data may hint at slightly higher temperatures (and thus deeper burial depths) for the side of the western La Panza Range closest to the Rinconda fault, but 40–50 °C is at the limit of what is measurable using these methods and cannot confidently be assigned any geologic significance.

TIMING AND MAGNITUDE OF EXTENSION AND SHORTENING

Following a period of mid-Tertiary tectonic quiescence, extension in the study area began with rapid deepening of the Salinas marine basin in late Saucesian to Luisian time. The Vaqueros, Monterey, and Santa Margarita Formations all thicken across the La Panza fault (Fig. 4), and the Saucesian-Relizian boundary at the top of the Vaqueros Formation (Fig. 4) records a shift to deeper-water, more anoxic conditions in the basin. We interpret normal slip on the La Panza fault and other normal faults to have begun in the late Saucesian, around 19 Ma or so. The lower part of the Santa Margarita Formation is cut by a syndepositional normal fault (Fig. 8), and the formation is overall thicker NE of the La Panza fault (Fig. 4), consistent with deposition of at least the lower part of it during faulting. Normal slip on the La Panza and related faults thus continued into the late Miocene, until sometime between 10 and 6 Ma. Whether extension was continuous from 19 Ma to 10–6 Ma or episodic within that interval is unclear, as is the timing of the transition from extension to shortening.

Vertical, normal-sense offset on the La Panza fault measured from stratigraphic, structural, and thermochronologic data is on the order of 1.4 km (Fig. 6), equivalent to roughly 600–900 m (1 km at most) of extension for an ~60° La Panza fault (Fig. 6). Another normal fault just west of the San Juan fault on section D-D′ (Fig. 6D) has ~900 m vertical normal-sense offset, or about ~400 m extension for the modeled fault dip. Overall, we estimate that total extension across the study area (perpendicular to the San Andreas fault) is on the order of 1 km, or ~2% strain at the scale of the ~50-km-wide Salinian block.

Both the La Panza (as a reverse fault) and Red Hills faults cut the Pleistocene Paso Robles Formation, which contains abundant clasts of recycled Monterey Formation (Galehouse, 1967) consistent with deposition during uplift and erosion of older rocks. Shortening was thus well under way by 3–4 Ma, consistent with the interpretations of Namson and Davis (1990) and Page et al. (1998). The Pliocene interval tentatively correlated with the Pancho Rico Formation in wells (Fig. 4) also contains reworked middle Miocene fauna (this study). It and the Paso Robles Formation together thicken NE to from <100 m to 2300 m in footwall of the Red Hills fault (Fig. 6A) and are thin or absent in its hanging wall. Similarly, both formations thicken NE from <100 m to ~700 m in the footwall of the La Panza fault and are thin to absent in its hanging wall (Figs. 4 and 6B). These relationships indicate that shortening perpendicular to the San Andreas fault probably began in the latest Miocene or earliest Pliocene (5–6) Ma. If (U-Th)/He ages of ca. 9 Ma from the eastern La Panza Range directly record the very earliest exhumation due to thrust slip on the La Panza fault, shortening may have begun as early as the late Miocene, although stratigraphic evidence for this is equivocal.

Vertical thrust-sense offset on the La Panza fault (and nearby faults) measured from stratigraphic, structural, and thermochronologic data is on the order of 1 to >2 km (Fig. 6), equivalent to 600–1400 m of shortening on a 60° La Panza fault. Seismic and gravity data indicate 2200–2800 m of shortening on the Red Hills fault (Figs. 6 and 7). Right-lateral slip on the San Juan fault at an oblique angle to the San Andreas fault may have resulted in another 500–1000 m of shortening by moving material out of the plane of the cross sections. Overall, we estimate that total shortening across the study area (perpendicular to the San Andreas fault) is on the order of 4 km, or ~10% strain at the scale of the ~50-km-wide Salinian block.

DISCUSSION

Kinematic Constraints on Extension and Shortening in the Central Coast Ranges

Data from our study area document mid-Tertiary tectonic quiescence, early to middle Miocene extension, and Pliocene and younger shortening. The transition from extension to shortening is poorly constrained between 10 and 5 Ma, and the overall magnitude of shortening is roughly 4–5 times greater than the amount of extension. These findings are broadly consistent with previous work from other Salinian block basins. Early to middle Miocene extension accommodated by high-angle faults has been documented in the northern Salinas Basin (Fig. 1) (Graham, 1978) and the Cuyama Basin (Fig. 1) (Lagoe, 1984; Davis et al., 1988; Yeats et al., 1989). The end of extension is indistinct, but crustal shortening was ongoing by ca. 4 Ma (e.g., Namson and Davis, 1990; Page et al., 1998). Compton (1966) estimated ~12% strain across the northern Salinian block, and Davis et al. (1988) found up to 50% strain (our estimate from their cross section) across the Cuyama Basin (although we question their structural assumptions; see next section). We suggest that these patterns of deformation in the central Coast Ranges are best understood in the context of their unusual overall tectonic boundary conditions, rather than as more local effects of transtension or transpression along the San Andreas fault.

The Salinian block is part of a triangular region bounded to the east by the San Andreas fault, to the west by the San Gregorio–Hosgri fault system, and to the south by the western Transverse Ranges (Fig. 11). The western Transverse Ranges block has rotated ~90° since 15 Ma, or up to 110° since 17 Ma (e.g., Hornafius et al., 1986; Luyendyk, 1991). Provided that the rotating block was effectively rigid (specifically, that its long axis did not change length) (e.g., Hornafius et al., 1986), and that the San Gregorio–Hosgri fault system was relatively close to its present trace in the middle Miocene (e.g., Dickinson et al., 2005), the width of the triangular region north of the rotating block would change over time in a predictable manner as the end of the rotating block moved way from, then toward, the San Andreas fault (Fig. 11). Assuming that the western Transverse Ranges rotated at a constant rate (Luyendyk, 1991), these boundary conditions predict rapid middle Miocene extension, a period of little to no deformation from 10 to 5 Ma, and shortening that increased from ca. 5 Ma to the present.

Strain compatibility with the western Transverse Ranges may explain why the transition from extension to shortening is difficult to resolve, even with detailed subsurface data—it took place gradually over a 5 m.y. interval in which very minor changes in slip or rotation rates could produce minor extension or shortening. The biggest problem is that the model predicts extension equal to or greater than the

Downloaded from lithosphere.gsapubs.org on September 21, 2012

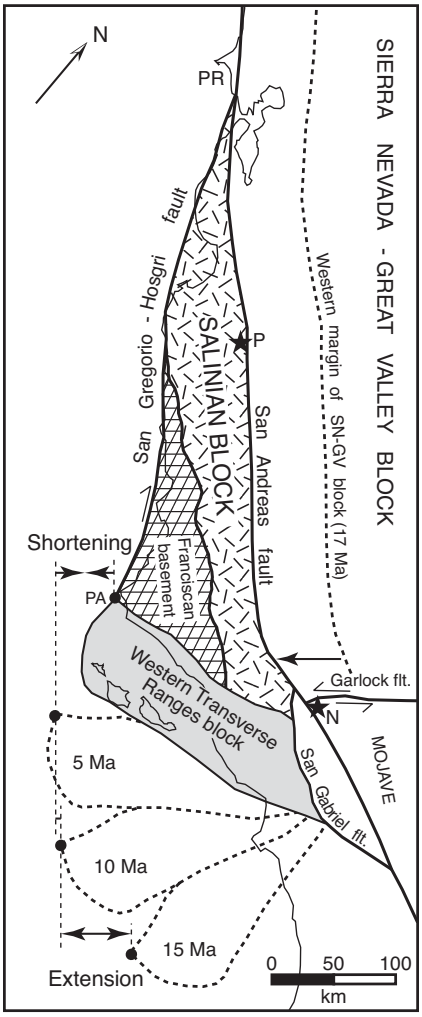

Figure 11. Sketch map showing tectonic elements of the central California Coast Ranges, based on Dickinson et al. (2005) and drawn from Jennings et al. (2010). P—Pinnacles volcanic field, N—Neenach volcanic field, PA—Point Arguello, PR—Point Reyes.

amount of shortening (Fig. 11), in contrast to the observation of much greater shortening. This discrepancy can be resolved by considering ~60 km of post–17 Ma left-lateral slip on the Garlock fault (Smith, 1962; Monastero et al., 1997), which resulted in westward motion of the Sierra Nevada–Great Valley block and development of the "big bend" in the San Andreas fault (Fig. 11). At 17 Ma, the Salinian block was mostly south of the Garlock fault, but it is now north of it due to slip on the San Andreas fault (Fig. 11). To first order, ~60 km of westward motion of the Sierra Nevada–Great Valley block over this interval nearly balance the amount of extension predicted by rotation of the western Transverse Ranges, although the way in which they compare at specific time intervals requires more detailed knowledge of time-varying slip rates on major faults.

Mechanics of Deformation within the Salinian Block

Namson and Davis (1988a, 1988b, 1990) and Davis et al. (1988) published interpretations of crustal shortening in the Coast Ranges based on the fault-bend fold principles of Suppe (1983), in which fault geometry at depth can be inferred from the geometry of folded (in this case Tertiary) sedimentary rocks at the surface. In their interpretation, both Salinian and Franciscan basement are deformed by moderately to gently dipping thrust faults that sole into subhorizontal brittle thrusts at depth; these thrust faults either cut and offset major strike-slip faults at depth—including the San Andreas fault—or are the major strike-slip faults (e.g., the Rinconada and San Gregorio–Hosgri faults). This style of deformation is characteristic of fold-and-thrust belts developed in layered sedimentary rocks, where elevated pore-fluid pressure allows thrust sheets to travel long distances along subhorizontal detachments parallel to bedding planes (e.g., Davis et al., 1983). It is not characteristic of homogeneous, nearly isotropic granitic basement like the Salinian block, which—lacking bedding planes and significant pore fluids—would be expected to deform more by the simple Mohr-Coulomb failure criteria first articulated by Anderson (1951), with high-angle (~60°) normal faults, lower-angle (~30°) reverse faults, and vertical strike-slip faults.

Geologic and geophysical data presented in this study demonstrate that the Salinian block in the study area deforms by simple "Andersonian"-style faulting, as close as any natural analogue might be expected to do. Miocene extension took place on high-angle normal faults, and Pliocene and younger shortening produced the ~30°-dipping Red Hills fault, while reactivating the existing La Panza fault. Strike-slip faults dip steeply in the brittle crust, and the San Andreas fault cuts the entire crust vertically to the Moho; normal and thrust faults are not observed to cut strike-slip faults. In our judgment, strict application of fault-bend fold models to the Salinian block should be critically reexamined, particularly in light of modern geophysical data sets that show strike-slip faults generally cutting the brittle crust at steep angles. Such models result in mechanically improbable fault geometries that may give an incorrect picture of the locations of potentially active faults in the subsurface. They may also overestimate the amount of shortening. For example, Davis et al.'s (1988) cross sections of the Cuyama Basin imply much greater shortening (~50%) than has been documented elsewhere in the Salinian block, and the calculation by Argus and Gordon (2001) of long-term Coast Range shortening rates found only half as much shortening as suggested by Namson and Davis (1988b).

CONCLUSIONS

The central Salinian block was deformed by early to middle Miocene extension, followed by Pliocene and younger shortening after a period of little to no deformation in the late Miocene. Extension was accommodated by high-angle normal faults, and shortening was accommodated by both new reverse faults and reactivation of older normal faults. The overall magnitude of shortening was roughly 4–5 times greater than the amount of extension. These findings are broadly consistent with previous work from other Salinian block basins, and we suggest that the entire block deformed in a similar manner over a similar time span. The timing and relative magnitude of extension and shortening can be understood in the context of local Coast Range boundary conditions linked to rotation of the western Transverse Ranges at the south end of the Salinian block. Older models for Coast Range shortening based on area-balanced fault-bend fold-style cross sections are a poor approximation of Salinian block deformation, and may lead to mechanically improbable fault geometries that overestimate the amount of shortening.

ACKNOWLEDGMENTS

This work was supported by the National Cooperative Geologic Mapping Program of the U.S. Geological Survey (USGS). We thank Carl Wentworth, Bob Jachens, Vicki Langenheim, Rick Stanley, and Earl Brabb of the USGS for sharing data and discussing interpretations, Sam Johnstone at the University of California–Santa Cruz for assistance with (U-Th)/He analyses, Trevor Dumitru at Stanford University for assistance with fission-track slide preparation, and Joe Wooden at Stanford University for assistance with U-Pb zircon analyses. Vicki Langenheim, Richard Stanley, and Carl Wentworth reviewed early versions of this manuscript, and the final version was significantly improved following suggestions from Steve Graham, Sarah Titus, and an anonymous reviewer.

APPENDICES

Appendix A: U-Pb SHRIMP Analytical Methods

Zircon concentrates were handpicked under a binocular microscope, and selected grains were

Downloaded from lithosphere.gsapubs.org on September 21, 2012

mounted in epoxy with the laboratory standard R33 (419 Ma) (Black et al., 2004) and polished with diamond compound to expose the midsections of the crystals. Polished grain mounts were imaged in reflected light with an optical microscope, gold-coated, and imaged in cathodoluminescence (CL) mode with a JEOL 5600 scanning electron microscope.

The SHRIMP ion microprobe at the Stanford–USGS Micro-Analytical Center (SUMAC) was operated with an O_2^- primary ion beam at ~6 nA, which produced a spot with a diameter of ~20–30 µm and a depth of 1–2 µm on the target zircons. Twenty-one peaks (plus background) were measured sequentially five times each (mass in parentheses): Y(89), La(139), Ce(140), Nd(146), Sm(147), Eu(153), Gd(155), DyO(179), ErO(182), YbO(188), Zr_2O(196), HfO(196), ^{204}Pb(204), ^{206}Pb(206), ^{207}Pb(207), ^{208}Pb(208), ^{232}Th(232), ^{238}U(238), ThO(248), UO(254), and UO_2(270). Data (Table A1; Fig. A1) were reduced following the methods described by Ireland and Williams (2003), using the SQUID and Isoplot programs of Ludwig (2001, 2003).

TABLE A1. ZIRCON U-Pb ANALYTICAL DATA

Spot name	Common ^{206}Pb (%)	U (ppm)	Th (ppm)	^{232}Th/^{238}U	^{206}Pb/^{238}U age* (Ma, ±1σ)	Total ^{238}U/^{206}Pb (%, ±1σ)	Total ^{207}Pb/^{206}Pb (%, ±1σ)
JC10-LP9, Western La Panza Range							
LP9-1.1	0.12	869	363	0.43	78.9 ± 0.7	81.2 ± 0.9	0.0485 ± 3.4
LP9-2.1	–0.11	1161	634	0.56	80.0 ± 0.6	80.1 ± 0.8	0.0467 ± 3
LP9-3.1	–0.07	745	345	0.48	76.5 ± 0.8	83.8 ± 1.0	0.047 ± 3.8
LP9-4.1	–0.09	1026	299	0.30	80.0 ± 0.7	80.2 ± 0.8	0.0469 ± 3.1
LP9-5.1	0.26	290	79	0.28	78.4 ± 1.3	81.5 ± 1.6	0.0496 ± 5.9
LP9-6.1	0.13	1683	793	0.49	80.5 ± 0.5	79.5 ± 0.6	0.0486 ± 2.4
LP9-7.1	–0.24	991	350	0.36	79.1 ± 0.7	81.1 ± 0.8	0.0457 ± 3.2
LP9-8.1	0.12	801	263	0.34	78.6 ± 0.8	81.5 ± 0.9	0.0485 ± 3.5
LP9-9.1	0.10	544	353	0.67	78.2 ± 0.9	81.9 ± 1.1	0.0484 ± 4.3
LP9-10.1	–0.15	1351	399	0.30	77.9 ± 0.6	82.4 ± 0.7	0.0464 ± 2.7
LP9-11.1	–0.19	1163	611	0.54	80.0 ± 0.6	80.2 ± 0.8	0.0461 ± 2.9
LP9-12.1	–0.05	471	95	0.21	76.5 ± 0.9	83.8 ± 1.2	0.0471 ± 4.5
LP9-13.1	0.03	889	408	0.47	75.8 ± 0.7	84.5 ± 0.9	0.0478 ± 3.4
LP9-14.1	–0.29	283	60	0.21	74.2 ± 1.1	86.7 ± 1.5	0.0452 ± 5.8
JC10-LP3, Eastern La Panza Range							
LP3-1.1	–0.21	548	368	0.69	80.3 ± 0.9	79.9 ± 1.0	0.0459 ± 3.9
LP3-2.1	0.05	921	441	0.49	79.6 ± 0.7	80.4 ± 0.8	0.0480 ± 3.1
LP3-3.1	–0.24	368	187	0.52	79.2 ± 1.1	81.1 ± 1.3	0.0457 ± 6.9
LP3-4.1	–1.50	84	28	0.34	78.6 ± 2.2	82.8 ± 2.8	0.0357 ± 11.9
LP3-5.1	0.18	542	175	0.33	77.4 ± 0.9	82.6 ± 1.1	0.0490 ± 4.0
LP3-6.1	0.31	314	77	0.25	77.5 ± 1.2	82.4 ± 1.5	0.0500 ± 5.3
LP3-7.1	0.31	882	176	0.21	80.1 ± 0.7	79.7 ± 0.9	0.0501 ± 3.1
LP3-8.1	–0.23	593	131	0.23	79.2 ± 1.1	81.0 ± 1.3	0.0457 ± 4.3
LP3-9.1	0.16	1645	675	0.42	79.2 ± 0.5	80.8 ± 0.7	0.0489 ± 2.4
LP3-10.1	–0.03	1687	2263	1.00	78.3 ± 0.5	81.8 ± 0.7	0.0473 ± 2.6
LP3-11.1	–0.02	1322	766	0.60	79.7 ± 0.6	80.4 ± 0.7	0.0474 ± 3.8
LP3-12.1	–0.11	792	208	0.27	78.9 ± 0.8	81.3 ± 1.0	0.0467 ± 3.6
LP3-13.1	–0.08	1128	417	0.38	76.8 ± 0.6	83.5 ± 0.7	0.0469 ± 2.8
LP3-14.1	0.19	989	340	0.36	76.9 ± 0.6	83.2 ± 0.8	0.0490 ± 3.0

*Corrected for ^{207}Pb.

Appendix B: Apatite Fission-Track Analytical Methods

Apatite grains were mounted in epoxy on glass slides and ground and polished by hand. Polished grain mounts were etched for 20 s in 5 *N* nitric acid at 22 °C and affixed to muscovite external detectors. Samples and external detectors were stacked single-file in plastic reactor cans and irradiated in the thermal column facility at the Oregon State University TRIGA reactor. CN5 dosimetry glasses with muscovite external detectors were used as neutron flux monitors (three per can). After irradiation, external detectors were etched in 48% HF.

Tracks were counted with a Zeiss Axioskop microscope with a 100× air objective, 1.25× tube factor, 10× eyepieces, and transmitted light with supplementary reflected light as needed. External detector prints were located with a Kinetek automated scanning stage (Dumitru, 1993). Only grains with *c* axes subparallel to the slide plane were dated. Ages were calculated using a zeta calibration factor of 367.6 ± 5.0 (e.g., Hurford and Green, 1983). Ages reported are the fission-track central age of Galbraith and Laslett (1993). Confined track lengths were measured only in apatite grains with *c* axes subparallel to slide plane; only horizontal tracks were measured (within ±5°–10°), following protocols of Laslett et al. (1982). Lengths were measured with computer digitizing tablet and drawing tube, calibrated against a stage micrometer (Dumitru, 1993). Confined track lengths were measured along with angles of tracks to the grains' *c* axes, following the protocols of Ketcham et al. (1999). Confined tracks hosted by surface tracks and by cleavage surfaces were both measured. Counting data are reported in Table B1, and track-length data are shown in Figure B1.

Appendix C: Apatite (U-Th)/He Analytical Methods

Apatite (U-Th)/He analyses were performed at the University of California–Santa Cruz. Dated

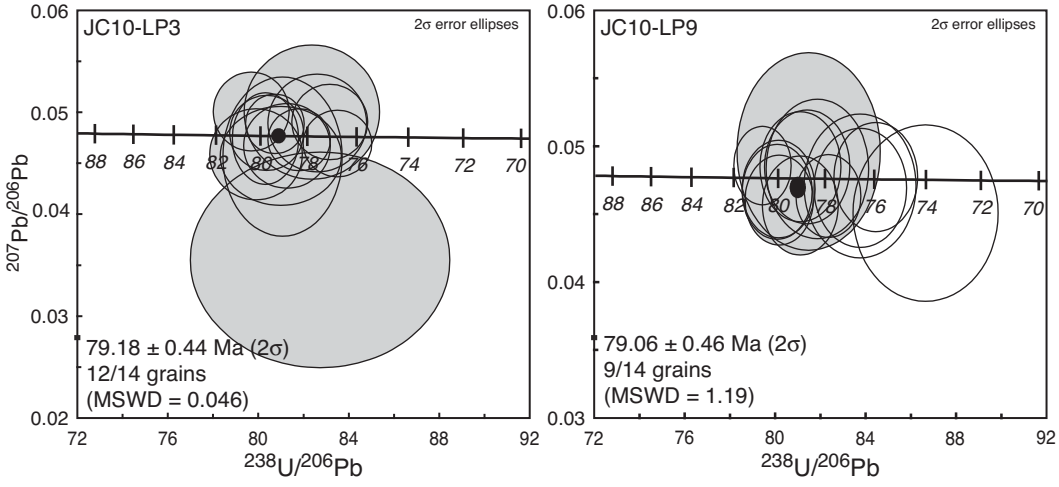

Figure A1. Concordia diagrams for U-Pb SHRIMP analyses. Open error ellipses omitted from age calculation, filled ellipses (gray) included. Black filled ellipse is the "Concordia age" calculated by Isoplot (Ludwig, 2001, 2003). MSWD—mean square of weighted deviates.

Downloaded from lithosphere.gsapubs.org on September 21, 2012

Table B1. Apatite Fission-track Counting Data

Sample number	Irradiation number	No. xls	Spontaneous		Induced		P(c2) (%)	Dosimeter		Age (Ma, ±1σ)
			Rho-S	NS	Rho-I	NI		Rho-D	ND	
JC10-LP1	SU078-01	28	0.4849	922	1.8186	3458	22.1	1.3800	4189	67.4 ± 3.1
JC10-LP2	SU078-02	23	0.3344	420	2.0725	2603	18.5	1.3775	4189	41.0 ± 2.5
JC10-LP3	SU078-03	19	0.4386	585	1.9382	2585	77.2	1.4076	4189	58.3 ± 2.9
JC10-LP4	SU078-04	21	0.4106	479	2.0197	2356	28.6	1.4076	4189	52.2 ± 3.2
JC10-LP5	SU078-05	18	0.3939	435	1.9080	2107	43.5	1.4377	4189	54.3 ± 3.1
JC10-LP6	SU078-06	19	0.4734	589	1.8935	2356	86.2	1.4377	4189	65.7 ± 3.3
JC10-LP7	SU078-07	14	0.8149	526	2.9993	1936	8.8	1.4978	4189	74.3 ± 4.8
JC10-LP9	SU078-09	18	0.5153	571	1.9915	2207	90.2	1.4828	4189	70.1 ± 3.6
JC10-LP11	SU078-011	22	0.4838	602	1.7994	2239	90.9	1.4978	4189	73.6 ± 3.7

Note: No. xls—number of individual crystals (grains) dated; Rho-S—spontaneous track density (×10^6 tracks per cm^2); NS—number of spontaneous tracks counted; Rho-I—induced track density in external detector (muscovite) (×10^6 tracks per cm^2); NI—number of induced tracks counted; P(χ^2)— χ^2 probability (Galbraith, 1981; Green, 1981); Rho-D—induced track density in external detector adjacent to dosimetry glass (×10^6 tracks per cm^2); ND—number of tracks counted in determining Rho-D; Age—"central age" (Galbraith and Laslett, 1993), calculated using zeta calibration (Hurford and Green, 1983) with zeta factor of 367.6 ± 5.0.

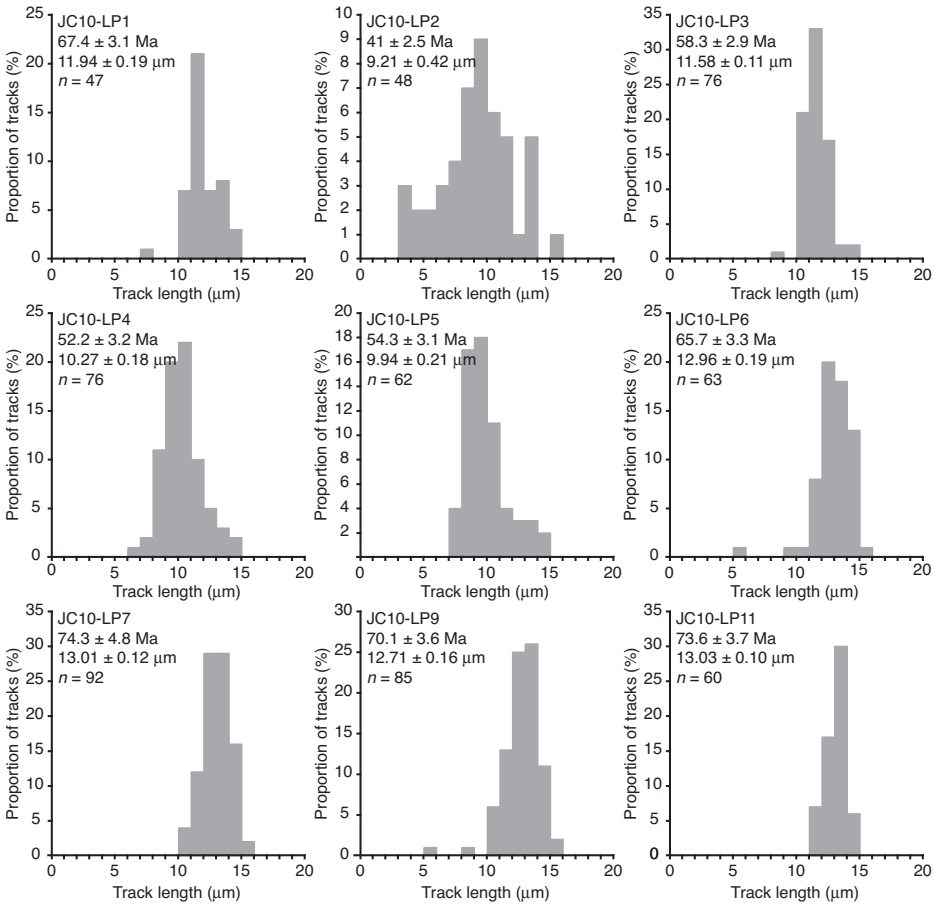

Figure B1. Fission-track length histograms. Data in upper left corner of each plot is (from top to bottom): Sample number, apparent fission-track age (±1σ), mean track length (±1σ), number of track-lengths measured.

apatite grains were handpicked from prepared mineral concentrates with a high-power (160×) stereo-zoom microscope with cross-polarization for screening inclusions. Individual crystals selected for analysis were digitally photographed and measured in at least two different orientations. Crystals were packaged in Nb foil tubes, which were loaded into a copper planchet and heated with a laser to ~1000 ± 25 °C for ~3 min to liberate He. Empty Nb packets (blanks) and fragments of the Durango apatite reference standard were analyzed using the same procedure.

After He extraction, individual packets were placed in polypropylene vials, spiked with ~25 mg of ~10 ppb ^{229}Th/^{233}U spike, and dissolved in concentrated nitric acid at ~100 °C for 3 h following protocols outlined by Reiners and Nicolescu (2006). After cooling, solutions were diluted with 2.5 mL of distilled water and analyzed within 24 h on an Element X-series II quadrapole inductively couple plasma–mass spectrometer (ICP-MS). Single-grain ages reported in Table C1 are alpha-ejection corrected to account for diffusion-domain-dependent loss of ^{4}He (Farley et al., 1996; Farley, 2002). Five replicate analyses of Durango apatite with an assumed age of 31.44 ± 0.18 Ma (McDowell et al., 2005) analyzed during the course of these analyses yielded a weighted-mean age of 30.11 ± 0.78 Ma (2σ).

Appendix D: Thermal Model Parameters

Thermal models (time-temperature paths) were generated using the HeFTy (v. 1.5.6) algorithm of Ketcham (2005). The following parameters were used for the fission-track model: Annealing model: "Ketcham et al. (2007a)"; *C*-axis projection: "Ketcham et al., 2007b"; Model *c*-axis-projected lengths: "Yes"; Default initial mean track length: "From Dpar"; Length reduction in standard: "0.893" (default); Kinetic parameter: "Dpar." Each sample was modeled using a single kinetic parameter (Dpar).

The following parameters were used for the (U-Th)/He model: Calibration: "Shuster et al. (2006) D_o/a^2 apatite"; Model precision: "Good"; Radius: Average radius of grains used to calculate a weighted-mean age for the sample (Table C1); Alpha calculation: "Static ejection"; Anneal traps?: "He loss"; Measured age (uncorrected): Defined such that the corrected age is equivalent to the mean (U-Th)/He age for the sample (Table C1); Age to report: "Corrected"; Alpha correction: "Ketcham et al. (in prep)"; Composition: Average U and Th of grains used to calculate the weighted-mean age of the sample (Table C1).

Inverse-modeling parameters for the combined fission-track and (U-Th)/He models were as follows: Search Method: Monte Carlo; Subsegment spacing: "Random"; Ending condition: Either "Paths tried = 5000" or "Good Paths = 50," whichever came first; Merit values: Good fit = 0.5, acceptable fit = 0.05. All segments are "monotonic consistent." Randomizer style is "Episodic." Number of path subdivisions ("halves") varied from model to model as appropriate.

REFERENCES CITED

Addicott, W.O., 1978, Revision of the age of the Pancho Rico Formation, central Coast Ranges, California: U.S. Geological Survey Bulletin 1457-A, p. A88–A89.

Addicott, W.O., Poore, R.Z., Barron, J.A., McDougall, K., and Gower, H.D., 1980, Miocene biostratigraphy of the Indian Creek–Shell Creek area, northern La Panza Range, San Luis Obispo County, California, *in* Blake, G.H., ed., Neogene Biostratigraphy of the Northern La Panza Range, San Luis Obispo County, California: Pacific Section, Society of Economic Paleontologists and Mineralogists, p. 11–38.

Anderson, E.M., 1951, The Dynamics of Faulting: Edinburgh, UK, Oliver and Boyd, 206 p.

Argus, D.F., and Gordon, R.G., 2001, Present tectonic motion across the Coast Ranges and San Andreas fault system in central California: Geological Society of America Bulletin, v. 113, no. 12, p. 1580–1592, doi:10.1130/0016-7606(2001)113<1580:PTMATC>2.0.CO;2.

Ballance, P.F., 1984, Sheet-flow dominated gravel fans of the non-marine middle Cenozoic Simmler Formation, central California: Sedimentary Geology, v. 38, p. 337–359, doi:10.1016/0037-0738(84)90085-X.

Downloaded from lithosphere.gsapubs.org on September 21, 2012

TABLE C1. APATITE (U-Th)/He ANALYTICAL DATA

Sample number	Grain number	Radius (μm)	Mass (μg)	U (ppm)	Th (ppm)	Th/U	He (mol × 10^{-14})	Ft	Age (Ma)	±1σ (Ma)
JC10-LP1	LP1a	84	14.0	9.1	5.0	0.56	0.53	0.82	8.3	0.2
	LP1b	110	27.8	11.3	8.1	0.72	1.55	0.86	9.1	0.2
	LP1c	80	11.7	8.6	5.9	0.69	0.58	0.81	11.4	0.3
		91		**10**	**6**				**9.6**	**0.3**
JC10-LP2	LP2a	~~77~~	~~13.8~~	~~17.6~~	~~25.2~~	~~1.44~~	~~3.23~~	~~0.81~~	~~22.5~~	~~0.4~~
	LP2b	103	28.5	28.6	20.4	0.71	4.00	0.86	9.1	0.2
	LP2c	100	24.6	21.7	21.3	0.98	4.05	0.85	13.4	0.2
		101		**25**	**21**				**11.2**	**0.4**
JC10-LP3	LP3a	83	18.3	14.4	20.8	1.45	2.37	0.83	14.9	0.3
	LP3b	112	26.6	25.3	15.4	0.61	4.79	0.86	13.4	0.2
	LP3c	68	8.3	20.6	16.5	0.8	0.86	0.79	9.9	0.2
		87		**20**	**18**				**12.7**	**0.3**
JC10-LP4	LP4a	95	22.3	15.6	19.6	1.25	1.87	0.84	9.1	0.4
	LP4b	103	19.8	21.9	23.1	1.06	2.64	0.84	10.7	0.3
	LP4c	74	9.9	22.4	24.3	1.09	1.37	0.80	11.4	5.6
		91		**20**	**22**				**10.4**	**0.4**
JC10-LP5	LP5a	74	14.4	8.1	10.7	1.32	0.67	0.81	10.0	0.4
	LP5b	85	15.6	18.2	21.7	1.20	1.44	0.82	8.9	0.3
	LP5c	53	5.9	12.5	25.0	2.00	0.41	0.74	9.4	0.4
		70		**13**	**19**				**9.4**	**0.4**
JC10-LP6	LP6a	77	11.4	14.6	20.8	1.42	3.94	0.81	40.4	1.3
	LP6b	79	13.9	10.4	15.8	1.51	3.07	0.81	35.3	1.1
	LP6c	grain was lost during analysis								
		78		**13**	**18**				**37.8**	**1.3**
JC10-LP7	LP7a	77	13.4	24.4	17.4	0.71	6.48	0.85	38.2	1.3
	LP7b	102	13.4	21.0	29.4	1.40	6.48	0.81	39.1	1.2
	LP7c	75	7.9	26.9	22.8	0.85	3.86	0.80	35.2	1.1
		84		**24**	**23**				**37.5**	**1.3**
JC10-LP9	LP9a	104	28.1	11.9	12.7	1.06	11.40	0.81	58.3	1.8
	LP9b	80	12.8	13.7	16.7	1.22	5.60	0.81	56.0	1.9
	LP9c	72	10.4	13.3	14.1	1.06	3.88	0.79	51.5	1.7
		85	**17.1**	**13**	**15**				**55.3**	**1.9**
JC10-LP11	LP11a	55	5.5	16.0	24.5	1.53	1.84	0.75	37.9	1.5
	LP11b	59	8.5	13.2	19.9	1.50	1.83	0.77	28.6	1.1
	LP11c	75	11.7	14.6	18.4	1.26	3.58	0.80	36.9	1.3
		63		**15**	**21**				**34.5**	**1.5**
Standard (Durango)	DUR1	–	–	–	–	18.4	14.10	–	31.6	0.9
	DUR2	–	–	–	–	18.7	4.09	–	30.4	0.6
	DUR3	–	–	–	–	18.7	4.10	–	29.7	0.5
	DUR4	–	–	–	–	17.8	6.15	–	30.1	0.6
	DUR5	–	–	–	–	19.5	17.20	–	29.4	0.8
									30.1	**0.8**

Note: Ft is the alpha-ejection correction of Farley (2002).Strike-through indicates grain omitted from mean age calculation.

Ballance, P.F., Howell, D.G., and Ort, K., 1983, Late Cenozoic wrench tectonics along the Nacimiento, South Cuyama, and La Panza faults, California, indicated by depositional history of the Simmler Formation, *in* Andersen, D.W., and Rymer, M.J., eds., Tectonics and Sedimentation along Faults of the San Andreas System: Los Angeles, California, Pacific Section, Society of Economic Paleontologists and Mineralogists, p. 1–9.

Barron, J.A., 1986, Paleoceanographic and tectonic controls on the deposition of the Monterey formation and related siliceous rocks in California: Palaeogeography, Palaeoclimatology, Palaeoecology, v. 53, p. 27–45.

Bartow, J.A., 1974, Sedimentology of the Simmler and Vaqueros Formations in the Caliente Range—Carrizo Plain Area, California: U.S. Geological Survey Open-File Report 74-338, 163 p.

Bartow, J.A., 1978, Oligocene continental sedimentation in the Caliente Range area, California: Journal of Sedimentary Petrology, v. 48, p. 75–98.

Black, L.P., Kamo, S.L., Allen, C.M., Davis, D.W., Aleinikoff, J.N., Valley, J.W., Mundil, R., Campbell, I.H., Korsch, R.J., Williams, I.S., and Foudoulis, C., 2004, Improved $^{206}Pb/^{238}U$ microprobe geochronology by the monitoring of a trace-element-related matrix effect: SHRIMP, ID-TIMS, ELA-ICP-MS, and oxygen isotope documentation for a series of zircon standards: Chemical Geology, v. 205, p. 115–140, doi:10.1016/j.chemgeo.2004.01.003.

Brabb, E.E., 2011, Location and Age of Foraminifer Samples Examined by Chevron Petroleum Company Paleontologists from more than 2,500 Oil Test Wells in California: U.S. Geological Survey Open-File Report, 2011-1262, 4 p.

Brocher, T.M., 2005, A regional view of urban sedimentary basins in northern California based on oil industry compressional-wave velocity and density logs: Bulletin of the Seismological Society of America, v. 95, p. 2093–2114, doi:10.1785/0120050025.

Burch, S.H., Grannell, R.B., and Hanna, W.F., 1971, Bouguer Gravity Map of California, San Luis Obispo Sheet: California Division of Mines and Geology, scale 1:250,000.

Campion, L.F., Chapman, R.H., Chase, G.W., and Youngs, L.G., 1983, Resource Investigation of Low- and Moderate-Temperature Geothermal Areas in Paso Robles, California: California Division of Mines and Geology Open-File Report 83-11 SAC, 113 p.

Chipping, D.H., 1972, Early Tertiary paleogeography of central California: American Association of Petroleum Geologists (AAPG) Bulletin, v. 56, p. 480–493.

Compton, R.R., 1966, Analysis of Pliocene-Pleistocene deformation and stresses in the northern Santa Lucia Range, California: Geological Society of America Bulletin, v. 77, p. 1361–1380, doi:10.1130/0016-7606(1966)77[1361:AOPDAS]2.0.CO;2.

Davis, D., Suppe, J., and Dahlen, F.A., 1983, Mechanics of fold-and-thrust belts and accretionary wedges: Journal of Geophysical Research, v. 88, p. 1153–1172, doi:10.1029/JB088iB02p01153.

Davis, T.L., Lagoe, M.B., Bazeley, W.J.M., Gordon, S., McIntosh, K., and Namson, J., 1988, Structure of the Cuyama Valley, Caliente Range, and Carrizo Plain and its significance to the structure of the southern Coast Ranges and westernmost Transverse Ranges, *in* Bazeley, W.J.M., ed., Tertiary Tectonics and Sedimentation in the Cuyama Basin, San Luis Obispo, Santa Barbara, and Ventura Counties, California: Pacific Section, Society of Economic Paleontologists and Mineralogists, v. 59, p. 141–158.

Dibblee, T.W., Jr., 1973a, Stratigraphy of the Southern Coast Ranges near the San Andreas Fault from Cholame to Maricopa, California: U.S. Geological Survey Professional Paper 764, 44 p.

Dibblee, T.W., Jr., 1973b, Regional Geologic Map of San Andreas and Related Faults in Carrizo Plain, Temblor, Caliente and La Panza Ranges and Vicinity, California: U.S. Geological Survey Miscellaneous Geologic Investigations Map I-757, scale 1:250,000.

Dibblee, T.W., Jr., 1976, The Rinconada and Related Faults in the Southern Coast Ranges, California, and Their Tectonic Significance: U.S. Geological Survey Professional Paper 981, 53 p.

Dibblee, T.W., Jr., 2004, Geologic Map of the Wilson Corner Quadrangle, San Luis Obispo County, California: Santa Barbara, California, Santa Barbara Museum of Natural History, Dibblee Geology Center Map DF-134, scale 1:24,000.

Dickinson, W.R., 1983, Cretaceous sinistral slip along Nacimiento fault in coastal California: Association of Petroleum Geologists (AAPG) Bulletin, v. 67, p. 624–645.

Dickinson, W.R., 1997, Tectonic implications of volcanism in coastal California: Geological Society of America Bulletin, v. 109, p. 936–954, doi:10.1130/0016-7606(1997)109<0936:OTIOCV>2.3.CO;2.

Dickinson, W.R., Ducea, M., Rosenberg, L.I., Green, H.G., Graham, S.A., Clark, J.C., Weber, G.E., Kidder, S., Ernst, W.G., and Brabb, E.E., 2005, Net Dextral Slip, Neogene San Gregorio-Hosgri Fault Zone, Coastal California: Evidence and Tectonic Implications: Geological Society of America Special Paper 391, 43 p.

Ducea, M.N., Kidder, S., Chesley, J.T., and Saleeby, J.B., 2009, Tectonic underplating of trench sediments beneath magmatic arcs, the central California example: International Geology Review, v. 51, p. 1–26, doi:10.1080/00206810802602767.

Dumitru, T.A., 1993, A new computer-automated microscope stage system for fission-track analysis: Nuclear Tracks and Radiation Measurements, v. 21, p. 575–580, doi:10.1016/1359-0189(93)90198-I.

Durham, D.L., 1974, Geology of the Southern Salinas Valley Area, California: U.S. Geological Survey Professional Paper 819, 111 p.

Downloaded from lithosphere.gsapubs.org on September 21, 2012

Durham, D.L., and Addicott, W.O., 1965, Pancho Rico Formation of Salinas Valley, California: U.S. Geological Survey Professional Paper 524-A, 22 p., 11 plates.

Farley, K.A., 2000, Helium diffusion from apatite: General behavior as illustrated by Durango flourapatite: Journal of Geophysical Research, v. 105, p. 2903–2914, doi:10.1029/1999JB900348.

Farley, K.A., 2002, (U-Th)/He dating: Techniques, calibrations, and applications: Reviews in Mineralogy and Geochemistry, v. 47, p. 819–844, doi:10.2138/rmg.2002.47.18.

Farley, K.A., Wolf, R.A., and Silver, L.T., 1996, The effect of long alpha-stopping distances on (U-Th)/He ages: Geochimica et Cosmochimica Acta, v. 60, p. 4223–4229, doi:10.1016/S0016-7037(96)00193-7.

Fuis, G.S., Scheirer, D.S., Langenheim, V.E., and Kohler, M.D., 2012, A new perspective on the geometry of the San Andreas fault in southern California and its relationship to lithospheric structure: BSSA (Bulletin of the Seismological Society of America), v. 102, no. 1, p. 236–251.

Galbraith, R.F., 1981, On statistical models for mixed fission-track ages: Nuclear Tracks and Radiation Measurements, v. 5, p. 471–478.

Galbraith, R.F., and Laslett, G.M., 1993, Statistical models for mixed fission-track ages: Nuclear Tracks and Radiation Measurements, v. 21, p. 459–470, doi:10.1016/1359-0189(93)90185-C.

Galehouse, J.S., 1967, Provenance and paleocurrents of the Paso Robles Formation, California: Geological Society of America Bulletin, v. 78, p. 951–978, doi:10.1130/0016-7606(1967)78[951:PAPOTP]2.0.CO;2.

Gleadow, A.J.W., Duddy, I.R., Green, P.F., and Lovering, J.F., 1986, Confined fission track lengths in apatite; a diagnostic tool for thermal history analysis: Contributions to Mineralogy and Petrology, v. 94, p. 405–415, doi:10.1007/BF00376334.

Graham, S.A., 1978, Role of the Salinian block in evolution of the San Andreas fault system: Association of Petroleum Geologists (AAPG) Bulletin, v. 62, p. 2214–2231.

Graham, S.A., 1987, Tectonic controls on petroleum occurrence in central California, *in* Ingersoll, R.V., and Ernst, W.G., eds., Cenozoic Basin Development in Coastal California: The Rubey Volume VI: Englewood Cliffs, New Jersey, Prentice-Hall, p. 47–63.

Graham, S.A., 1989, Oligocene and Miocene paleogeography of central California and displacement along the San Andreas fault: Geological Society of America Bulletin, v. 101, p. 711–730, doi:10.1130/0016-7606(1989)101<0711:OAMPOC>2.3.CO;2.

Green, P.F., 1981, A new look at statistics in fission-track dating: Nuclear Tracks and Radiation Measurements, v. 5, p. 77–86.

Green, P.F., Duddy, I.R., Laslett, G.M., Hegarty, K.A., Gleadow, A.J.W., and Lovering, J.F., 1989, Thermal annealing of fission tracks in apatite: 4. Quantitative modeling techniques and extension to geological time scales: Chemical Geology–Isotope Geoscience Section, v. 79, p. 155–182, doi:10.1016/0168-9622(89)90018-3.

Grove, K., 1993, Latest Cretaceous basin within the Salinian terrane of west-central California: Geological Society of America Bulletin, v. 105, p. 447–463, doi:10.1130/0016-7606(1993)105<0447:LCBFWT>2.3.CO;2.

Hardebeck, J.L., 2010, Seismotectonics and fault structure of the California central coast: Bulletin of the Seismological Society of America, v. 100, p. 1031–1050, doi:10.1785/0120090307.

Hardebeck, J.L., 2012, Fluid-driven seismicity response of the Rinconada fault near Paso Robles, California, to the 2003 M6.5 San Simeon earthquake: Bulletin of the Seismological Society of America, v. 102, p. 377–390.

Hart, E.W., 1976, Basic Geology of the Santa Margarita Area, San Luis Obispo County, California: California Division of Mines and Geology Bulletin 199, 45 p.

Hornafius, J.S., Luyendyk, B.P., Terres, R.R., and Kamerling, M.J., 1986, Timing and extent of Neogene tectonic rotation of the western Transverse Ranges, California: Geological Society of America Bulletin, v. 97, p. 1476–1487, doi:10.1130/0016-7606(1986)97<1476:TAEONT>2.0.CO;2.

Hurford, A.J., and Green, P.F., 1983, The zeta age calibration in fission-track dating: Chemical Geology, v. 41, p. 285–317, doi:10.1016/S0009-2541(83)80026-6.

Ireland, T.R., and Williams, I.S., 2003, Considerations in zircon geochronology by SIMS, *in* Hanchar, J.M., and Hoskin, P.W.O., eds., Zircon: Reviews in Mineralogy and Geochemistry, v. 53, p. 215–241.

Jacobson, C.E., Grove, M., Pedrick, J.N., Barth, A.P., Marsaglia, K.M., Gehrels, G.E., and Nourse, J.A., 2011, Late Cretaceous–early Cenozoic tectonic evolution of the southern California margin inferred from provenance of trench and forearc sediments: Geological Society of America Bulletin, v. 123, p. 485–506, doi:10.1130/B30238.1.

Jennings, C.W. (with modifications by Gutierrez, C., Bryant, W., Saucedo, G., and Willis, C.), 2010, Geologic Map of California: California Geological Survey Geologic Data Map 2, scale 1:750,000.

Ketcham, R.A., 2005, Forward and inverse modeling of low-temperature thermochronometry data, *in* Reiners, P.W., and Ehlers, T.A., eds., Low-Temperature Thermochronology: Techniques, Interpretations, and Applications: Reviews in Mineralogy and Geochemistry, v. 58, p. 275–311.

Ketcham, R.A., Donelick, R.A., and Carlson, W.D., 1999, Variability of apatite fission-track annealing kinetics: 3. Extrapolation to geological time scales: The American Mineralogist, v. 84, p. 1235–1255.

Lagoe, M.B., 1984, Paleogeography of the Monterey Formation, Cuyama Basin, California: American Association of Petroleum Geologists Bulletin, v. 68, no. 5, p. 610–627.

Laslett, G.M., Kendall, W.S., Gleadow, A.J.W., and Duddy, I.R., 1982, Bias in the measurements of fission-track length distributions: Nuclear Tracks and Radiation Measurements, v. 6, p. 79–85, doi:10.1016/0735-245X(82)90031-X.

Ludwig, K.R., 2001, Squid: A Users' Manual: Berkeley Geochronology Center Special Publication 2, 19 p.

Ludwig, K.R., 2003, Isoplot 3.00: A Geochronological Toolkit for Excel: Berkeley Geochronology Center Special Publication 4, 67 p.

Luyendyk, B.P., 1991, A model for Neogene crustal rotations, transtension, and transpression in southern California: Geological Society of America Bulletin, v. 103, p. 1528–1536, doi:10.1130/0016-7606(1991)103<1528:AMFNCR>2.3.CO;2.

Mattinson, J.M., and James, E.W., 1985, Salinian block U-Pb age and isotopic variations: Implications for origin and emplacement of the Salinian terrane, *in* Howell, D.G., ed., Terranes of the Circum-Pacific Region: Circum-Pacific Council for Energy and Mineral Resources Earth Science Series 1, p. 215–226.

McDougall, K., 2007, Chapter 4, California Cenozoic biostratigraphy—Paleogene, *in* Scheirer, A.H., ed., Petroleum Systems and Geologic Assessment of Oil and Gas in the San Joaquin Basin Province, California: U.S. Geological Survey Professional Paper 1713, 56 p.

McDowell, F.W., McIntosh, W.C., and Farley, K.A., 2005, A precise $^{40}Ar/^{39}Ar$ reference age for the Durango apatite (U-Th)/He and fission-track dating standard: Chemical Geology, v. 214, p. 249–263, doi:10.1016/j.chemgeo.2004.10.002.

McPhee, D.K., Langenheim, V.E., and Watt, J.T., 2011, Preliminary Isostatic Residual Gravity Anomaly Map of Paso Robles 30 × 60 Minute Quadrangle, California: U.S. Geological Survey Open-File Report 2011-1104, scale 1:100,000, and data table (http://pubs.usgs.gov/of/2011/1104/).

Monastero, F.C., Sabin, A.E., and Walker, J.D., 1997, Evidence for post–early Miocene initiation of movement on the Garlock fault from offset of the Cudahy Camp Formation, east-central California: Geology, v. 25, p. 247–250, doi:10.1130/0091-7613(1997)025<0247:EFPEMI>2.3.CO;2.

Morelli, C., ed., 1974, The International Gravity Standardization Net, 1971: International Association of Geodesy Special Publication 4, 194 p., and Pan-American Center for Earth and Environmental Studies, 2010, http://gis.utep.edu/ (last accessed 1 June 2010).

Namson, J., and Davis, T., 1988a, Structural transect of the western Transverse Ranges, California: Implications for lithospheric kinematics and seismic risk evaluation: Geology, v. 16, p. 675–679, doi:10.1130/0091-7613(1988)016<0675:STOTWT>2.3.CO;2.

Namson, J., and Davis, T., 1988b, Seismically active fold-thrust belt in the San Joaquin Valley, central California: Geological Society of America Bulletin, v. 100, p. 257–273, doi:10.1130/0016-7606(1988)100<0257:SAFATB>2.3.CO;2.

Namson, J., and Davis, T., 1990, Fold and thrust belt of the southern Coast Ranges and Santa Maria Basin, California: American Association of Petroleum Geologists (AAPG) Bulletin, v. 74, p. 467–492.

Page, B.M., 1970, Sur-Nacimiento fault zone of California: Continental margin tectonics: Geological Society of America Bulletin, v. 81, p. 667–690, doi:10.1130/0016-7606(1970)81[667:SFZOCC]2.0.CO;2.

Page, B.M., Wagner, H.C., McCulloch, D.S., Silver, E.A., and Spotts, J.H., 1979, Tectonic interpretation of a geologic section of the continental margin off San Luis Obispo, the southern Coast Ranges, and the San Joaquin Valley, California: Cross-section summary: Geological Society of America Bulletin, v. 90, p. 808–812, doi:10.1130/0016-7606(1979)90<808:TIOAGS>2.0.CO;2.

Page, B.M., Thompson, G.A., and Coleman, R.G., 1998, Late Cenozoic tectonics of the central and southern Coast Ranges of California: Geological Society of America Bulletin, v. 110, p. 846–876, doi:10.1130/0016-7606(1998)110<0846:OLCTOT>2.3.CO;2.

Parsons, T., McCarthy, J., Hart, P.E., Hole, J.A., Childs, J., Oppenheimer, D.H., and Zoback, M.L., 2002, A review of faults and crustal structure in the San Francisco Bay area as revealed by seismic studies: 1991–97, *in* Parsons, T., ed., Crustal Structure of the Coastal and Marine San Francisco Bay Region, California: U.S. Geological Survey Professional Paper 1658, p. 119–145.

Powell, R.E., 1993, Balanced palinspastic reconstruction of pre–late Cenozoic paleogeography, southern California, *in* Powell, R.E., Weldon, R.J., II, and Matti, J.C., eds., The San Andreas Fault System: Displacement, Palinspastic Reconstruction, and Geologic Evolution: Geological Society of America Memoir 178, p. 1–106.

Reiners, P.W., and Nicolescu, S., 2006, Measurement of Parent Nuclides for (U/Th)/He Chronometry by Solution Sector ICP-MS: Tucson, University of Arizona, ARDHL (Arizona Radiogenic Helium Dating Laboratory) Report 1, 33 p.

Rosenberg, L.I., and Clark, J.C., 2009, Map of the Rinconada and Reliz Fault Zones, Salinas River Valley, California: U.S. Geological Survey Scientific Investigations Map 3059, scale 1:250,000, 27 p.

Ross, D.C., 1966, Granitic and Gneissic Rocks near the San Andreas Fault from Bodega Head to Cajon Pass, California: U.S. Geological Survey Professional Paper 698, 92 p.

San Luis Obispo County Water Resources Division of Public Works, 2005, Paso Robles Groundwater Basin Study Phase II: Numerical Model Development, Calibration, and Application: prepared by Fugro West Inc., ETIC Engineering Inc., and Cleath and Associates, http://www.SLOCountyWater.org/site/Water%20Resources/Reports/Paso%20Phase%202/index.htm (last accessed January 2012).

Shelly, D.R., 2010, Migrating tremors illuminate complex deformation beneath the seismogenic San Andreas fault: Nature, v. 463, p. 648–652, doi:10.1038/nature08755.

Smith, G.I., 1962, Large lateral displacement on Garlock fault, California, as measured from offset dike swarm: American Association of Petroleum Geologists (AAPG) Bulletin, v. 46, p. 85–104.

Spotila, J.A., House, M.A., Niemi, N.A., Brady, R.C., Oskin, M., and Buscher, J.T., 2007, Patterns of bedrock uplift along the San Andreas fault and implications for mechanisms of transpression, *in* Till, A.B., Roeske, S.M., Sample, J.C., and Foster, D.A., eds., Exhumation Associated with Continental Strike-Slip Fault Systems: Geological Society of America Special Paper 434, p. 15–33, doi:10.1130/2007.2434(02).

Suppe, J., 1983, Geometry and kinematics of fault-bend folding: American Journal of Science, v. 283, p. 684–721, doi:10.2475/ajs.283.7.684.

Tagami, T., and O'Sullivan, P.B., 2005, Fundamentals of fission-track thermochronology, *in* Reiners, P.W., and Ehlers, T.A., eds., Low-Temperature Thermochronology: Techniques, Interpretations, and Applications: Reviews in Mineralogy and Geochemistry, v. 58, p. 2–47.

Thurber, C., Zhang, H., Waldhauser, F., Hardebeck, J., Michael, A., and Ebhart-Phillips, P., 2006, Three-dimensional

Downloaded from lithosphere.gsapubs.org on September 21, 2012

wavespeed model, earthquake relocations, and focal mechanisms for the Parkfield, California, region: Bulletin of the Seismological Society of America, v. 96, p. 38–49, doi:10.1785/0120050825.

Titus, S.J., Dyson, M., DeMets, C., Tikoff, B., Rolandone, F., and Bürgmann, R., 2011, Geologic versus geodetic deformation adjacent to the San Andreas fault, central California: Geological Society of America Bulletin, v. 123, p. 794–820, doi:10.1130/B30150.1.

Toké, N.A., Arrowsmith, J.R., Rymer, M.J., Landgraf, A., Haddad, D.E., Busch, M., Coyan, J., and Hannah, A., 2011, Late Holocene slip rate of the San Andreas fault and its accommodation by creep and moderate-magnitude earthquakes at Parkfield, California: Geology, v. 39, p. 243–246, doi:10.1130/G31498.1.

Trehu, A.M., and Wheeler, W.H., 1987a, A Seismic Refraction Profile across the Coast Ranges of Central California—Morro Bay to the San Andreas Fault: U.S. Geological Survey Miscellaneous Field Studies Map MF-1920.

Trehu, A.M., and Wheeler, W.H., 1987b, Possible evidence for subducted sedimentary materials beneath central California: Geology, v. 15, p. 254–258, doi:10.1130/0091-7613(1987)15<254:PEFSSM>2.0.CO;2.

Vedder, J.G., and Brown, R.D., 1968, Structure and stratigraphic relationship relations along the Nacimiento fault in the southern Santa Lucia Range and San Rafael Mountains, California, *in* Dickinson, W.R., and Grantz, A., eds., Proceedings of a Conference on Geologic Problems of the San Andreas Fault System: Stanford University Publications in the Geological Sciences 11, p. 242–259.

Vedder, J.G., McLean, H., Stanley, R.G., and Wiley, T.J., 1991, Paleogeographic implications of an erosional remnant of Paleogene rocks southwest of Sur-Nacimiento fault zone, southern Coast Ranges, California: Geological Society of America Bulletin, v. 103, p. 941–952, doi:10.1130/0016-7606(1991)103<0941:PIOAER>2.3.CO;2.

Wakabayashi, J., Hengesh, J.V., and Sawyer, T.L., 2004, Four-dimensional fault processes: Progressive evolution of step-overs and bends: Tectonophysics, v. 392, p. 279–301, doi:10.1016/j.tecto.2004.04.013.

White, L.A., 1992, Thermal and Unroofing History of the Western Transverse Ranges, California: Results from Apatite Fission-Track Thermochronology [Ph.D. thesis]: Austin, Texas, University of Texas at Austin, 299 p.

Williams, C.F., D'Alessio, M.A., Grubb, F.V., and Galanis, S.P., 2005, Heat flow studies in the SAFOD main hole: Eos (Transactions, American Geophysical Union), abstract T23E-07.

Wolf, R.A., Farley, K.A., and Silver, L.T., 1996, Helium diffusion and low-temperature thermochronometry of apatite: Geochimica et Cosmochimica Acta, v. 60, p. 4231–4240, doi:10.1016/S0016-7037(96)00192-5.

Wolf, R.A., Farley, K.A., and Kass, D.M., 1998, Modeling of the temperature sensitivity of the apatite (U-Th)/He thermochronometer: Chemical Geology, v. 148, p. 105–114.

Yeats, R.S., Calhoun, J.A., Nevins, B.B., Schwing, H.F., and Spitz, H.M., 1989, Russell fault: Early strike-slip fault of California Coast Ranges: American Association of Petroleum Geologists (AAPG) Bulletin, v. 73, p. 1089–1102.

Zeitler, P.K., Herczeg, A.L., McDougall, I., and Honda, M., 1987, U-Th-He dating of apatite: A potential thermochronometer: Geochimica et Cosmochimica Acta, v. 51, p. 2865–2868, doi:10.1016/0016-7037(87)90164-5.

MANUSCRIPT RECEIVED 26 FEBRUARY 2012
REVISED MANUSCRIPT RECEIVED 4 JUNE 2012
MANUSCRIPT ACCEPTED 6 JUNE 2012

Printed in the USA